The effect of sudden wind shear on the Earth's magnetosphere: Statistics of wind shear events and CCMC simulations of magnetotail disconnections

Joseph E. Borovsky[1,2]

Received 14 February 2012; revised 24 April 2012; accepted 6 May 2012; published 22 June 2012.

[1] The solar wind is filled with strong current sheets and sudden velocity shears; often the two are co-located. Sudden velocity shears at 1 AU are statistically analyzed using ACE measurements from 1998 to 2008. The occurrence rates of passage and the orientations of the shear planes are examined. For shear layers with vector velocity changes $|\Delta \underline{v}| > 50$ km/s, an average of ~12 pass the Earth per day. In the fast wind, ~60 sudden shear layers pass the Earth per day (about 2.5 per hour). To explore the effects of sudden wind shears on the Earth's magnetosphere, global magnetospheric MHD simulations with four different simulation codes are performed at the Community Coordinated Modeling Center (CCMC) with north-south and east-west wind shears. Windsock movement of the magnetotail is analyzed and comet-like disconnections of the magnetotail and magnetosheath are examined. Sudden changes in the cross-polar-cap potential and ionospheric Joule dissipation are seen as the shear layers pass the Earth. Other potential effects of sudden wind shear on the magnetosphere are discussed.

Citation: Borovsky, J. E. (2012), The effect of sudden wind shear on the Earth's magnetosphere: Statistics of wind shear events and CCMC simulations of magnetotail disconnections, *J. Geophys. Res.*, *117*, A06224, doi:10.1029/2012JA017623.

1. Introduction

[2] Abrupt velocity shears are ubiquitous in the solar wind plasma [*Burlaga*, 1968; *Neugebauer et al.*, 1984; *Borovsky*, 2008] and many shear layers per day pass the Earth's magnetosphere. The abrupt shears (vorticity layers) separate different blocks of solar wind plasma that move at different velocity [*Borovsky*, 2006]. Across the shear layers the abrupt change $\Delta \underline{v}$ in the vector flow $\underline{v}$ of the solar wind is typically accompanied by an abrupt change $\Delta \underline{B}$ in the solar wind magnetic field direction, i.e., there is a current sheet co-located with the velocity shear. These magnetic field changes are better studied [e.g., *Vasquez et al.*, 2007], where they are known in the space-physics literature as solar wind discontinuities [*Siscoe et al.*, 1968; *Tsurutani and Ho*, 1999]. The focus here, however, will be on the velocity shear.

1.1. What the Velocity Shears Are

[3] The origin of the strong velocity shears in the solar wind is not known. Several ideas have been discussed in the literature.

[4] The strong shear layers could be boundaries between wiggling tubes of magnetized plasma [*Bruno et al.*, 2001; *Borovsky*, 2008, 2010]. Supporting this notion, the solar wind plasma is born in magnetic flux tubes [cf. *Fisk and Zurbuchen*, 2006, Figure 2; *Pariat et al.*, 2009, Figure 1]. The flux tube picture can account for the evolution of the spread of magnetic field directions about the Parker spiral with distance from the Sun and the anisotropy of the magnetic field directions in corotating interaction regions [*Borovsky*, 2010]. Further support for this notion will come from section 2 where it will be shown that the velocity shears often separate plasmas with different specific entropies. A question about this explanation is why the wigglings of the plasma tubes are Alfvenic?

[5] The strong shear layers could be steepened Alfven waves propagating out from the Sun [*Malara et al.*, 1996; *Vasquez and Hollweg*, 1999; *Tsurutani and Ho*, 1999; see also *Gosling et al.*, 2011]. The fact that a good portion of the shears are very Alfvenic ($\underline{v}$ and $\underline{B}$ perturbations are correlated, with amplitude ratios corresponding to outward-traveling Alfven waves) supports this notion. The fact that many of these shears are co-located on plasma density, temperature, and/or composition boundaries argues against this notion.

[6] The strong shear layers could be vorticity sheets generated within MHD turbulence [*Miller et al.*, 1996; *Mininni et al.*, 2006; *Greco et al.*, 2009]. Sheets of vorticity are seen in computer simulations of turbulence, co-located [*Mininni et al.*, 2006] or not co-located [*Miller et al.*, 1996] with current sheets. Arguing against this notion, the amplitudes of the sheets of interest in the solar wind are extremely large ($|\Delta \underline{v}| \sim v_A$ as will be shown in section 2). Also, expectations

[1]Space Science Institute, Boulder, Colorado, USA.
[2]Also at Department of Atmospheric, Oceanic and Space Sciences, University of Michigan, Ann Arbor, Michigan, USA.

Corresponding author: J. E. Borovsky, Space Science Institute, 4750 Walnut St., Boulder, CO 80301, USA. (jborovsky@spacescience.org)

©2012. American Geophysical Union. All Rights Reserved.
0148-0227/12/2012JA017623

from simulations are that the layers should have thicknesses at the dissipation scale [*Biskamp and Welter*, 1989; *Dmitruk et al.*, 1998; *Lazarian and Vishniac*, 1999; *Maron and Goldreich*, 2001] whereas in the solar wind they are much thicker.

[7] The strong shear layers could be discontinuities formed by the relaxation of tangled magnetic fields [*Longcope and Strauss*, 1993; *Parker*, 1994, 2004]. This relaxation usually applies to magnetic field lines that are tied at both ends, whereas the solar wind is tied only at one end; hence tangling could lead to propagation without relaxation into discontinuities in the solar wind. Two questions about this explanation are why the discontinuities should have shears and why the discontinuities should be outward-traveling Alfvenic.

[8] The strong shear layers could be remnants from chromospheric jets [*Feldman et al.*, 1993; *Yamauchi et al.*, 2003]. Arguing for this notion is the fact that jetting flows are detected some distance from the Sun [e.g., *Wang et al.*, 1998; *DeForest et al.*, 2001; *Gabriel et al.*, 2003]. Arguing against this notion is the fact that at 1 AU the vector jump $\Delta\underline{v}$ across the shear tends to avoid the radial direction (see section 2).

[9] One more explanation for strong shear layers that should be explored is "zonal flows." Zonal flows with velocities up to 0.5 v_A are known to spontaneously form in unstable laboratory plasmas owing to nonlinear energy transfer from turbulence [*Diamond et al.*, 2005; *Itoh et al.*, 2006; *Naulin et al.*, 2005]. In the laboratory plasmas the shear flows are often referred to as "transport barriers" [*Burrell*, 1997; *Terry*, 2000] owing to the local suppression of turbulence at the shear layer. An investigation of zonal-flow physics for the conditions of the solar wind plasma has not been performed.

1.2. Importance of Strong Shear Layers for the Solar Wind

[10] The solar wind protons [*Marsch et al.*, 1982; *Schwartz and Marsch*, 1983; *Freeman and Lopez*, 1985; *Richardson et al.*, 1995] and electrons [*Pilipp et al.*, 1990; *Phillips et al.*, 1995] are heated with distance from the Sun. It has long been recognized that the free energy of differential flow is a possible source for in situ heating of the solar wind plasma [*Coleman*, 1968; *Parker*, 1969]. Potential mechanisms for solar wind heating associated with velocity shears are dissipation of Kelvin-Helmholtz waves [*Korzhov et al.*, 1985; *Neugebauer et al.*, 1986], the excitation and dissipation of MHD turbulence [*Roberts et al.*, 1992; *Goldstein*, 2009], the phase mixing of Alfven waves [*Ruderman et al.*, 1999; *Kaghashvili*, 1999], damping of MHD surface waves [*Hollweg et al.*, 1990; *Yang and Hollweg*, 1991], damping of shear-driven plasma waves [*Migliuolo*, 1984; *Markovskii et al.*, 2006], and Landau-damping of the shear structure itself [*Borovsky and Gary*, 2009, 2011]. However, no heating was found in the long-lived large-scale shears of corotating interaction regions [cf. *Borovsky and Denton*, 2010a, Figures 4 and 9] where sheared slow wind keeps its specific entropy low). Heating at intense small-spatial-scale shears is another issue [cf. *Borovsky and Denton*, 2011].

[11] Velocity shear in the solar wind is also of interest as a potential driver for MHD turbulence [*Coleman*, 1968; *Belcher and Davis*, 1971; *Roberts et al.*, 1992; *Goldstein et al.*, 1999]. Driving of solar wind turbulence by Kelvin-Helmholtz-like instabilities in shear zones has been explored [*Korzhov et al.*, 1984; *Roberts et al.*, 1992; *Malara*, 1999], as has the driving of solar wind turbulence by shearing low-frequency Alfven waves [*Roberts et al.*, 1987, 1992; *Grappin and Velli*, 1996; *Ghosh et al.*, 1998; *Roberts and Ghosh*, 1999] and by the reflection of outward-traveling Alfven waves off shear structures [*Bavassano and Bruno*, 1992; *Klein et al.*, 1993]. A statistical study of the properties of solar wind fluctuations in the vicinity of corotating-interaction-region shear zones at 1 AU found no evidence for the production of turbulence [*Borovsky and Denton*, 2010a].

[12] The abrupt velocity shears of the solar wind appear to defy the action of eddy viscosity [*Borovsky*, 2006], which should broaden the shear layers. The concept of eddy viscosity, which is well established experimentally for shear in Navier–Stokes fluids, is thought to be valid for MHD fluids with a mean magnetic field [cf. *Chen and Montgomery*, 1987; *Yoshizawa and Yokoi*, 1996; *Ishizawa and Hattori*, 1998] but with complications owing to the anisotropy of the fluctuations, to the fluid memory provided by the field, and to the Alfvenic propagation of shear along the mean field. Attempts to calculate an eddy-viscosity coefficient for the solar wind from observations of the velocity fluctuations have resulted in values that differ by 8 orders of magnitude [*Korzhov et al.*, 1984, 1985; *Verma*, 1996; *Borovsky*, 2006]. For the collisionless solar wind, *Borovsky and Gary* [2009, 2011] explored methods to calculate shear viscosities from Bohm diffusion and from Landau damping, which yield values below those of eddy-viscosity estimates. Bohm-diffusion calculations give shear-layer thicknesses at 1 AU of few thousand kilometers, which is in the ballpark of thicknesses observed with the high-time-resolution plasma measurements from the Wind spacecraft. It is also in the ballpark of the thickness of number-density transitions on plasma boundaries at 1 AU.

1.3. The Effect of Solar Wind Discontinuities on the Magnetosphere

[13] For years it has been suspected that "northward turnings" of the solar wind magnetic field can trigger magnetospheric substorms [e.g., *Rostoker*, 1983; *Lyons et al.*, 1996; *Hsu and McPherron*, 2006] (but see *Morley and Freeman* [2007] and *Freeman and Morley* [2009] for evidence against this). These northward turnings occur as solar wind current sheets pass the Earth, and solar wind current sheets typically have co-located velocity shear layers. Hence, sudden wind shear effects may have been hidden in these previous studies of solar wind triggering by sudden magnetic field changes, but the effects of the wind shears were not separately studied. Assessing the separate importance of magnetic field changes and velocity-vector changes on the stability of the magnetosphere should be done.

[14] A solar wind discontinuity with the proper orientation can interact with the Earth's bow shock to produce a "hot flow anomaly" [*Thomsen et al.*, 1986; *Schwartz et al.*, 2000; *Facskó et al.*, 2008] wherein solar wind ions that reflect off the bow shock travel upstream inside the discontinuity and produce a rapid pressure expansion of the discontinuity's current sheet [*Burgess*, 1989; *Thomas et al.*, 1991; *Koval et al.*, 2005]. Hot flow anomalies are known to produce large transient outward displacements of the magnetopause

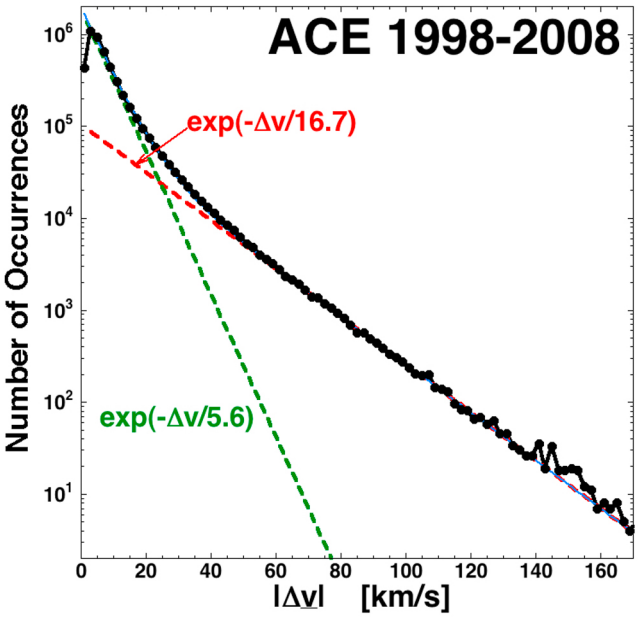

Figure 1. The occurrence distribution of the 64-s change $|\Delta\underline{v}| = |\underline{v}(t) - \underline{v}(t\text{-}64\ s)|$ in the solar wind velocity vector for all plasma measurements in the ACE 1998–2008 data set. The distribution is fit by two exponential functions.

[*Safrankova et al.*, 2000; *Sibeck et al.*, 2000], transient brightenings of the morning and afternoon aurora [*Sibeck et al.*, 1999; *Fillingim et al.*, 2011], traveling convection vortices in the ionosphere [*Sibeck et al.*, 1999; *Fillingim et al.*, 2011], and magnetospheric Pc3 oscillations [*Eastwood et al.*, 2011].

[15] An outstanding issue for high-speed-stream-driven geomagnetic-storm physics and the radiation-belt energization that occurs during these storms is the importance or not of the Alfvenic solar wind fluctuations in high-speed streams [cf. *Denton et al.*, 2008]. *Tsurutani and Gonzalez* [1987] argued that the time-varying magnetic field of the solar wind associated with the Alfvenic fluctuations produces enhanced driving of the magnetosphere. It was later suggested (1) that the efficiency of reconnection is greater during the strongly southward intervals of magnetic field than it would be if the field were steady [*Gonzalez et al.*, 2006], (2) that the switching on and off of reconnection between the solar wind and the magnetosphere by the fluctuating magnetic fields launches Alfven-wave transients inside the magnetosphere that result in impulsive uplifts of ionospheric plasma [*Tsurutani et al.*, 2006], and (3) that intermittent southward solar wind magnetic fields produce intermittent strong convection in the magnetosphere that in turn produces magnetospheric plasma waves (dawnside whistler chorus) that act to energize the electron radiation belt [*Lyons et al.*, 2009]. Other studies, on the contrary, argue that the value of the time-averaged magnetic field during the storm is of the primary importance over the fact that the field may wildly fluctuate [*McPherron et al.*, 2009; *Liemohn et al.*, 2011]. In such studies of the effects of steady versus fluctuating magnetic fields, assessing the roles of the strong velocity shears that accompany the magnetic field changes should be considered.

1.4. This Investigation

[16] This investigation aims to determine the properties of shear layers in the solar wind and to investigate the effects that those solar wind velocity shears may have on the Earth's magnetosphere.

[17] This report is organized as follows. In section 2 the statistical properties of velocity shear layers in the solar wind are investigated and in section 3 the basic properties of wind shears are laid out. In section 4 global MHD simulations of the solar wind-driven magnetosphere-ionosphere system of the Earth are performed to discern the reaction of that system to sudden wind shears. Section 4.1 looks at the advection of the velocity shear layers though the magnetosheath to make contact with the magnetopause. Section 4.2 looks at the re-orientation of the bow shock and the magnetopause in response to the velocity shear. Section 4.3 looks at the movement and disconnection of the Earth's magnetotail caused by the velocity shear. Section 4.4 looks at the change in ionospheric currents in response to the velocity shear. Section 5 contains discussions about the potential impacts that sudden wind shears may have on the Earth's magnetosphere, on the comet analogy for the reaction of the magnetotail, and on future simulations and data-analysis projects that are needed.

2. Statistics of Sudden Wind Shears

[18] In Figure 1 the change Δv in the vector flow velocity $\underline{v}$ of the solar wind every 64 s is binned for the 1998–2008 ACE data set at 1 AU, defined as $\Delta v \equiv |\Delta\underline{v}| = |\underline{v}(t) - \underline{v}(t\text{-}64\ s)|$. The proton velocity-vector measurements are from the SWEPAM instrument [*McComas et al.*, 1998]. Two populations can be seen in the distribution: a population of small changes (fit by the green exponential $\exp(-\Delta v/5.6)$) and a population of large changes (fit by the red exponential $\exp(-\Delta v/16.7)$). The sum of the two exponential functions (blue curve) well describes the distribution of occurrences. The distribution of large Δv occurrences represents a population of strong velocity shears in the solar wind. The two distributions are clearly separated at $\Delta v = 40$ km/s.

[19] In Table 1 the average number of strong shear events per day at Earth is tabulated from the 1998–2008 ACE data set. The wind is separated into slow wind ($v_{sw} \le 425$ km/s) and fast wind ($v_{sw} \ge 600$ km/) in the table; in this separation by speed, the fast wind contains mostly plasma of coronal-hole origin and ejecta and the slow wind contains plasma of coronal-hole origin, non-coronal-hole origin, and ejecta [cf. *Borovsky*, 2012a]. Note in Table 1 that strong shear

Table 1. The Occurrence Rates of Sudden Velocity Shears in the ACE 1998–2008 Data Set of 64-s Differences at 1 AU[a]

	Slow Wind $v_{sw} \le 425$ km/s	Fast Wind $v_{sw} \ge 600$ km/s	All Wind
$\Delta v > 40$ km/s	3.9 per day	102 per day	24.7 per day
$\Delta v > 50$ km/s	1.6 per day	57 per day	12.4 per day
$\Delta v > 60$ km/s	0.69 per day	32 per day	6.6 per day
$\Delta v > 70$ km/s	0.32 per day	18.7 per day	3.6 per day
$\Delta v > 80$ km/s	0.15 per day	10.5 per day	2.0 per day
$\Delta v > 90$ km/s	0.065 per day	5.9 per day	1.1 per day
$\Delta v > 100$ km/s	0.037 per day	3.4 per day	0.60 per day

[a]Here, $\Delta v \equiv |\Delta\underline{v}| = |\underline{v}(t) - \underline{v}(t\text{-}64\ s)|$.

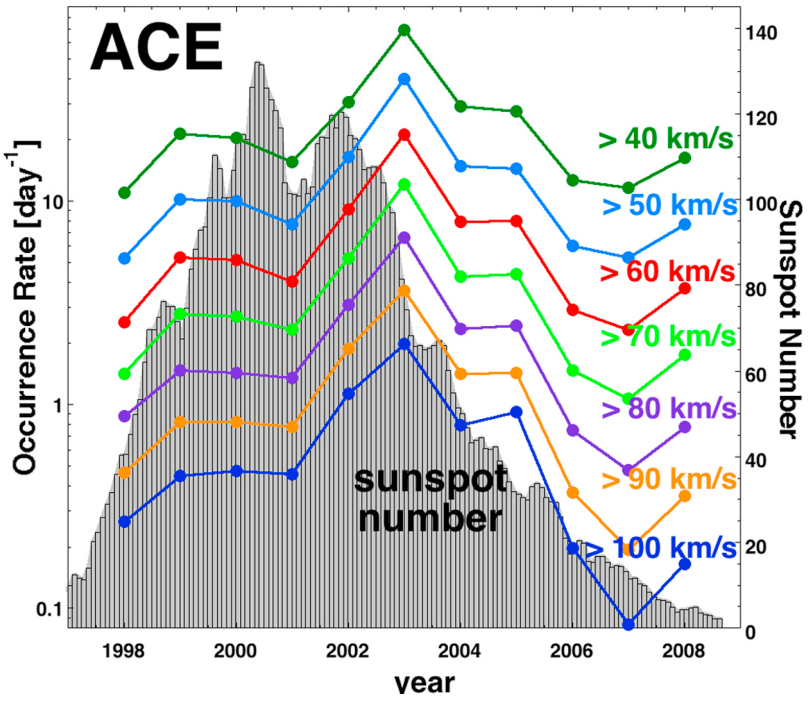

Figure 2. The yearly averaged daily occurrence rate for strong shear layers passing the Earth is plotted (colors, left axis) for the years 1998–2008 as measured by the ACE spacecraft at 1 AU. The different colors (labeled) are for different thresholds for identifying a velocity-shear layer. The black histogram (right axis) is the six-month-averaged averaged sunspot number.

events occur at a far higher rate in fast solar wind than in slow solar wind. This is consistent with the finding [*Borovsky*, 2008; *Borovsky and Denton*, 2010a] that the density of discontinuities is higher in the fast wind than in the slow wind, plus the fact that fast wind sweeps structure past the Earth at a higher rate than does slow wind, plus the fact that the magnetic discontinuities of the slow wind tend to have weaker velocity shears than do comparable magnetic discontinuities of the fast wind. As can be seen in Table 1, for all types of solar wind for $\Delta v > 40$ km/s there are on average ~25 shear events per day passing the Earth, for $\Delta v > 50$ km/s there ~12 events per day, for $\Delta v > 60$ km/s there ~7 per day, for $\Delta v > 80$ km/s there ~2 per day, and for $\Delta v > 100$ km/s there ~0.6 per day.

[20] In Figure 2 the average occurrence frequency of strong shear events at Earth is plotted year by year for 1998–2008 as determined from the ACE data set. The five colored curves pertain to different levels of wind shear events from $\Delta v > 40$ km/s to $\Delta v > 100$ km/s. Also plotted on Figure 2 (gray, right axis) is the sunspot number. As can be seen in Figure 2 the occurrence frequency of sudden velocity shears varies substantially from year to year, presumably in part because the mix of slow and fast wind (and ejecta) varies from year to year. The year with the highest occurrence rates of wind shear events is 2003, early in the declining phase of the solar cycle. The year 2003 was characterized by strong, long-lasting high-speed streams [e.g., *Tripathi et al.*, 2007] and a large amount of ejecta [cf. *Zhao et al.*, 2009, Figure 1].

[21] To look at the properties of strong velocity shears in the solar wind we will take $\Delta v > 60$ km/s in 64 s to be the working definition of a "strong" shear. Taking the definition $\Delta v > 60$ km/s results in 23,875 strong shears in the 1998–2009 ACE data set. In Table 2 some of the properties of this collection of strong shears are listed. These are indeed strong shears: the mean value of Δv is 78 km/s, the mean value of $\Delta v/v_A$ is 1.03, and the mean value of $\Delta v/C_{ms}$ is 0.77. This latter ratio indicates that the magnetosonic Mach number of the shear is of order unity.

[22] The strong velocity shears in the solar wind are co-located with current sheets [cf. *Borovsky*, 2008, Figure 4]: in Table 2 the mean 64-s angular change in the magnetic field direction $\Delta\theta_B$ is 60° for the 23,875 strong shears in the ACE data set.

[23] It has been shown that the strong current sheets in the solar wind are often co-located on plasma boundaries [cf. *Borovsky*, 2008, Figure 5; 2012b, Figure 6]; since the

Table 2. Some Properties of the Collection of 23,875 Strong Shears ($|\Delta v| > 60$ km/s) in the 1998–2008 ACE Data Set[a]

Symbol	Quantity	Value
$\Delta\underline{v}$	Vector jump of the solar wind velocity across the shear	78 ± 19 km/s
$\Delta\theta_v$	Angular change of solar wind velocity vector across the shear	6.7° ± 2.3°
$\Delta\theta_B$	Angular change of magnetic field vector across the shear	60° ± 31°
$\Delta\underline{B}$	Vector jump in the magnetic field across the shear	6.9 ± 3.8 nT
$\Delta v/v_A$	Velocity jump across the shear relative to Alfven speed	1.03 ± 0.53
$\Delta\underline{v}/C_{ms}$	Velocity jump across the shear relative to magnetosonic speed	0.77 ± 0.24

[a]The numbers listed are mean values ± standard deviations.

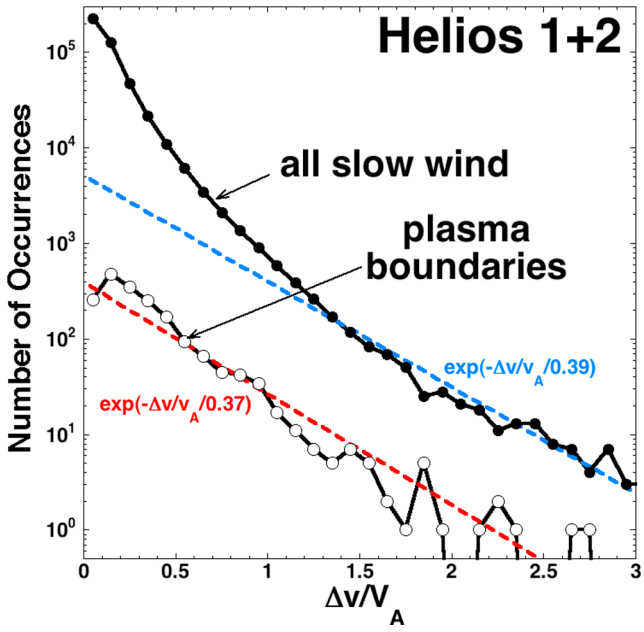

Figure 3. The top curve is the occurrence distribution of the 80-s change $\Delta v/v_A$ in the solar wind velocity vector for all slow-wind measurements in the Helios 1 and 2 data subintervals and the bottom curve is the occurrence distribution of $\Delta v/v_A$ for measurements at plasma interfaces in the slow wind. Note $\Delta v \equiv |\Delta \underline{v}| = |\underline{v}(t) - \underline{v}(t\text{-}64\ s)|$.

strong velocity shears are often co-located with strong current sheets this implies that strong velocity shears can be co-located with plasma boundaries. This co-location is directly shown in Figure 3 where a collection of plasma boundaries [from *Borovsky*, 2012b] in the Helios 1 and Helios 2 slow-wind data sets are analyzed. The plasma boundaries are located via strong temporal jumps in the proton specific entropy $S_p = T_p/n_p^{2/3}$, the proton number density n_p, or the proton beta $\beta_p = 8\pi n_p k_B T_p/B^2$ measured with plasma [*Rosenbauer et al.*, 1977] and magnetic field [*Denskat and Neubauer*, 1982] instruments on Helios 1 and Helios 2 from 0.31 to 0.98 AU. The top curve in Figure 3 plots the occurrence distributions of 80-s changes $\Delta v/v_A$ for the entire Helios 1 and 2 slow-wind data sets and the bottom curve plots the occurrence distributions of 80-s changes $\Delta v/v_A$ at the plasma boundaries. As can be seen, the upper curve shows the dual population of weak changes and of strong changes in the solar wind whereas the lower curve shows only the population of strong changes. Selecting plasma boundaries selects shear layers. Hence, plasma boundaries in the solar wind have strong velocity shears co-located with them.

[24] These current-sheet velocity-shears in the solar wind are commonly referred to as solar wind discontinuities [*Siscoe et al.*, 1968; *Tsurutani and Ho*, 1999; *Vasquez et al.*, 2007]. Traditionally, solar wind discontinuities have been classified as rotational discontinuities and tangential discontinuities [*Burlaga*, 1969; *Burlaga and Ness*, 1969; *Turner and Siscoe*, 1971]; recent studies, however, indicate that they are predominantly tangential discontinuities [*Horbury et al.*, 2001; *Knetter et al.*, 2003, 2004; *Riazantseva et al.*, 2005a, 2005b; see also *Burlaga*, 1971], which are plasma boundaries. It is well known that the solar wind discontinuities exhibit velocity changes along with the magnetic field changes and it has been pointed out that these changes at the discontinuities are Alfvenic [*Neugebauer et al.*, 1984, 1986; *Neugebauer*, 1985], i.e., that the properties of the velocity changes and the properties of the magnetic field changes are correlated.

[25] Using the cross-product method [*Burlaga and Ness*, 1969; *Knetter et al.*, 2004] on the magnetic field change across discontinuities, the orientations of the normals $\underline{n}$ to the shear layers are examined. The direction of the unit normal $\underline{n}$ is obtained via $\underline{n} = \underline{B}_1 \times \underline{B}_2/|\underline{B}_1 \times \underline{B}_2|$ where $\underline{B}_1$ and $\underline{B}_2$ are the magnetic field vectors on the two sides of the current sheet (on the two sides of the velocity-shear layer). Only strong shears ($\Delta v > 60$ km/s) that had magnetic field direction changes $\Delta\theta_B > 30°$ were used to calculate the normal directions. In Figure 4 the density of unit normals on the unit sphere is viewed from above the ecliptic plane (Figure 4, top) and from along the Parker-spiral direction (Figure 4, bottom). As can be seen, the Parker-spiral direction organizes the shear-layer orientations wherein the normals tend to be perpendicular to the Parker-spiral direction and quasi-isotropic about the Parker spiral. (The shear-plane orientations are consistent with the boundaries of magnetic or plasma tubes aligned with the Parker spiral [*Borovsky*, 2008].)

[26] Even though the normal directions of the shear layers are organized by the Parker-spiral direction, the velocity-jump directions are not. The vector velocity jumps $\Delta \underline{v} = \underline{v}(t) - \underline{v}(t\text{-}64\ s)$ tend to be transverse to the radial direction, rather than transverse to the Parker-spiral direction (see also *Klein et al.* [1991, 1993] in contrast to *Belcher and Davis* [1971]). For the collection of 23,875 velocity shears with $\Delta v > 60$ km/s, the RMS values of the three RTN velocity components are $\Delta v_r = 35.1$ km/s, $\Delta v_t = 47.2$ km/s, and $\Delta v_n = 54.5$ km/s. (The Rotational-Tangential-Normal coordinate system [cf. *Alevizos et al.*, 1999]) has R as the vector direction from the Sun to the spacecraft, T being the direction of the cross product of the Sun's angular-momentum vector with the R direction, and N being the R cross T direction.) Rotating into the nominal Parker-spiral reference frame the RMS values of the three components become $\Delta v_{\parallel} = 38.8$ km/s, $\Delta v_{\perp} = 44.2$ km/s, and $\Delta v_n = 54.5$ km/s where $\parallel$ indicates parallel to the Parker-spiral direction in the ecliptic plane and $\perp$ indicates perpendicular to the Parker-spiral direction in the ecliptic plane. Rotating into the Parker-spiral direction does not minimize the averaged Δv component in the direction parallel to the Parker spiral.

[27] The orientation of a shear plane is typically not aligned with the orientation of nearby shear planes, i.e., nearby shear planes are not parallel to each other. (There are exceptions where a sequence of current sheets can be parallel, including the multiple current sheets near sector reversals [*Nakagawa et al.*, 1989; *Nakagawa*, 1993; *Crooker et al.*, 1993, 1996] and the multiple shear layers inside corotating interaction regions where the plasma is compressed in one direction flattening out magnetic structures [*Borovsky*, 2006, 2010].) Using the cross-product method to determine the orientation of magnetic shear layers in the solar wind in the ACE data set from 1998 to 2004, the vector change in normal

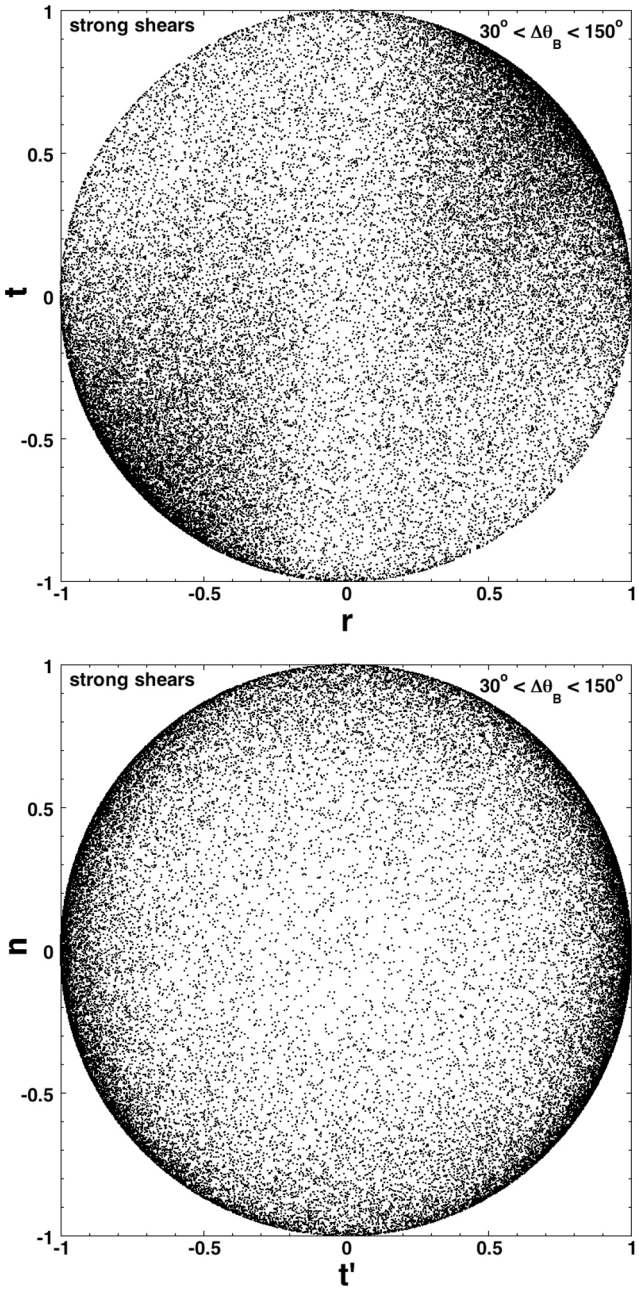

Figure 4. Unit vector normals to planes of strong shear in the solar wind at 1 AU. (top) The unit vectors from above the ecliptic plane (where the Parker spiral goes from upper left to lower right); (bottom) the unit vectors from along the Parker spiral.

direction from one layer to the next layer is measured and binned in Figure 5. The solid points are the measurements of the difference angle in three dimensions and the hollow points are the difference in the azimuthal angles for the projections of the normal directions perpendicular to the Parker-spiral direction. The angles are measured in a fashion from 0° to 90°. The mean value for the difference angle from one layer to the next in three dimensions is 36.6° and the mean difference angle in the azimuth angle perpendicular to the Parker spiral from one layer to the next is 32.0°. Hence, when multiple shear layers are passing the Earth, the orientation from one shear layer to the next will differ substantially.

[28] The shear planes of the solar wind are not infinite in extent. At 1 AU the transverse-to-radial correlation length of the solar wind is on the order of 50–100 R_E [*Richardson and Paularena*, 2001; see also *Weimer and King*, 2008]. Figure 5 along with the non-infiniteness of the planes yields a picture of the plane structure of the solar wind like the one sketched in *Borovsky* [2008, Figure 1] where the planes create a cellular decomposition of the solar wind [cf. *Schliecker*, 2002]. That cellular picture applies to both the slow and the fast wind, with some differences. In the slow wind the cells are bigger than in the fast wind [*Borovsky*, 2008]. (See also the parameter N_d in *Borovsky* [2012a, Table 4] where the sheets are counted in fast wind, slow wind, coronal-hole-origin wind, non-coronal-hole-origin wind, and ejecta.) In the slow wind the plasma tends to differ in density and temperature from cell to cell with abrupt changes across the cell boundaries (magnetic and shear planes) whereas in the fast wind the plasma properties have little variation. The cell boundaries in the slow wind tend to have strong magnetic field rotations but weak velocity shears whereas in the fast wind the boundaries are nearly Alfvenic with strong magnetic rotations and velocity jumps.

[29] The strong vector velocity jumps $\Delta\underline{v}$ in the solar wind that are being analyzed are indeed shears. This is confirmed by determining the normal direction $\underline{n}$ of the shear layer and checking to see that vector $\Delta\underline{v}$ is normal to the $\underline{n}$. Using the magnetic field change across the layer with the cross product method, the unit vector $\underline{n}$ normal to plane is obtained. In Figure 6 for the ACE velocity jumps with good magnetic field perturbations the distribution of angles between $\Delta\underline{v}$ and $\underline{n}$ is plotted. As can be seen in Figure 6 the average angle tends toward 90°, meaning $\Delta\underline{v}$ is a velocity shear. (This was

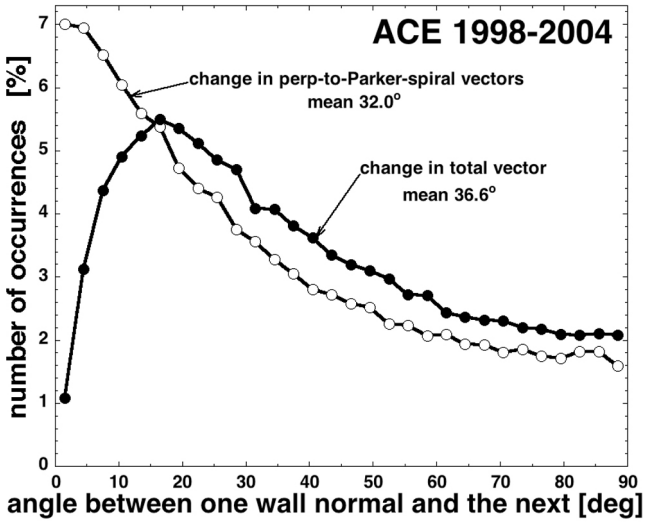

Figure 5. Every time a shear plane is crossed by ACE, the normal vector to the plane is calculated. Here the change in the normal direction from one plane to the next is binned.

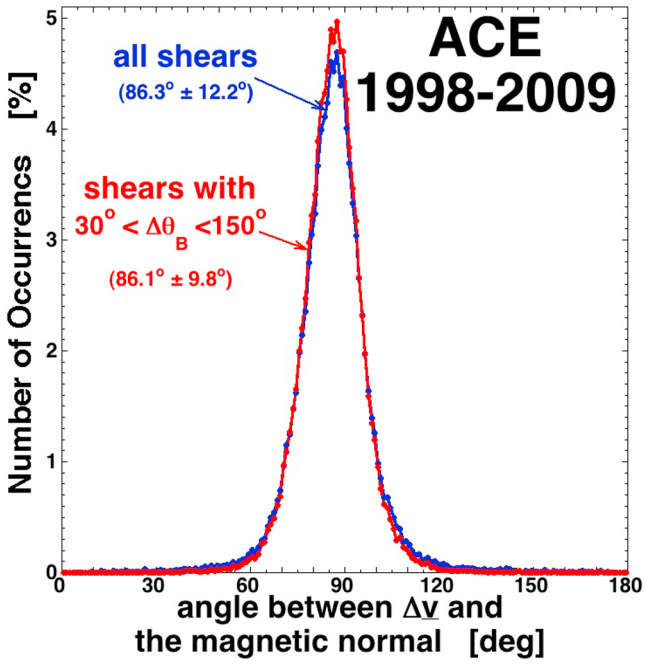

Figure 6. The angle between the normal to a shear layer $\underline{n}$ (as determined from the magnetic perturbation using the cross-product method) and the direction of the velocity change $\Delta\underline{v}$ across the shear is binned for 20,039 of the 23,875 strong shears.

to be expected since signatures of compression such as changes in $|\underline{B}|$ or nk_BT would be obvious if the strong $\Delta\underline{v}$ were not shears.)

3. Alfvenic Wind Shears

[30] As noted in section 2, a velocity shear is almost always accompanied by a current sheet: the properties of the two are related in specific ways. I.e., the changes $\Delta\underline{v}$ across the shear and the change $\Delta\underline{B}$ across the current sheet are not independent.

[31] Particularly in the fast (coronal-hole-origin) solar wind [cf. *Borovsky and Denton*, 2010a, Figure 13], discontinuities are Alfvenic with velocity and magnetic field changes that are correlated in the sense of outward-propagating Alfvnenic perturbations. Since (a) the normals of the discontinuities are perpendicular to the ambient magnetic field and (b) the group velocity of Alfvenic perturbations is ducted parallel to the magnetic field [*Fejer and Lee*, 1967; *Goertz and Boswell*, 1979], it is not clear whether there is any actual propagation associated with the Alfvenic shear layers in the solar wind.

[32] For the shear layers in the solar wind, there are constraints on $\Delta\underline{v}$ and $\Delta\underline{B}$ related to the toward-away sector structure of the wind and to the type of solar wind. For pure outward-propagating Alfvenic perturbations, the changes $\Delta\underline{v}$ and $\Delta\underline{B}$ are related by $\Delta\underline{v} = -\Delta\underline{b} = -\Delta\underline{B}/(4\pi nm_i)^{1/2}$ when the IMF is outward (away sector) and $\Delta\underline{v} = +\Delta\underline{b} = +\Delta\underline{B}/(4\pi nm_i)^{1/2}$ when the IMF is inward (toward sector). In the highly Alfvenic fast wind these two relations can be taken as approximately true for strong velocity shears. In the less-Alfvenic slow wind the satisfaction of these two conditions is weaker, with $|\Delta\underline{v}| < |\Delta\underline{b}|$ in general. Further constraining $\Delta\underline{v}$ and $\Delta\underline{B}$ in the shear layers, $|\Delta\underline{v}|$ must be perpendicular to $\underline{n}$, where $\underline{n}$ is the normal of the shear layer, which is also the normal to the current sheet. There is a further tendency for $\Delta\underline{v}$ to be perpendicular to radial rather than perpendicular to the Parker-spiral direction while $\Delta\underline{B}$ has the tendency to be perpendicular to the Parker-spiral direction.

4. Reaction of the Earth's Magnetosphere to Sudden Wind Shear

[33] Numerical simulations of the reaction of the Earth's magnetosphere are performed with the LFM [*Lyon et al.*, 2004; *Wiltberger et al.*, 2005] version LTR-2_1_1, the BATSRUS [*Powell et al.*, 1999; *De Zeeuw et al.*, 2000; *Gombosi et al.*, 2000] version 8.01, the GUMICS [*Janhunen et al.*, 2012] version 4-HC-1.11, and the Open-GGCM [*Raeder*, 1999; *Raeder et al.*, 2001] version 3.1 MHD computer codes at the Community Coordinated Modeling Center (CCMC) [*Bellaire*, 2004, 2006]. A set of simulations with the four codes are all run with the same solar wind conditions: these solar wind parameters are listed in Table 3. The solar wind parameters are steady throughout the simulation, except for v_z, which is $v_z = -40$ km/s for the first 2 h of the simulation and then it is suddenly switched to $v_z = +40$ km/s wherein it is held steady for 2 more hours. Following those 4 simulations, two others are run with the LFM code; for those two simulations the solar wind speed v_x is reduced from -450 km/s to -300 km/s and the shear is increased from ± 40 km/s to ± 50 km/s, with the shear in v_z in one run and the shear in v_y in the other.

4.1. Advection of the Velocity-Shear Layer Through the Earth's Magnetosheath

[34] As the velocity shear layer in the solar wind passes the Earth and its magnetosphere, a nonzero amount of time is required for the shear layer to be advected through the magnetosheath behind the bow shock before the shear layer makes contact with the Earth's magnetopause. This delay in the contact time is demonstrated in Figures 7a–7d, taken from an LFM simulation of the interaction of a velocity shear layer with the Earth's magnetosphere. Figures 7a–7d are equatorial-plane (Z = 0) cuts of the simulation system at four different times; the color plotted is the v_z component of the plasma flow velocity with v_z negative (southward,

Table 3. The Standard Solar Wind Conditions for the MHD Simulations of This Investigation[a]

Symbol	Value	Quantity
n	6 cm^{-3}	solar wind plasma number density
v_x	−450 km/s	solar wind x velocity
v_y	0 km/s	solar wind y velocity
v_z	±40 km/s	solar wind z velocity
B_x	0 nT	solar wind x-component of magnetic field
B_y	5 nT	solar wind y-component of magnetic field
B_z	0 nT	solar wind z-component of magnetic field
T	7 eV	solar wind plasma temperature
v_A	44 km/s	Alfven speed in the solar wind
C_s	24 km/s	sound speed in the solar wind
C_{ms}	50 km/s	magnetosonic speed in the solar wind
M_{ms}	9	magnetosonic Mach number of solar wind

[a]The simulations are run first with $v_z = -40$ km/s and then are switched to $v_z = +40$ km/s across the wind shear.

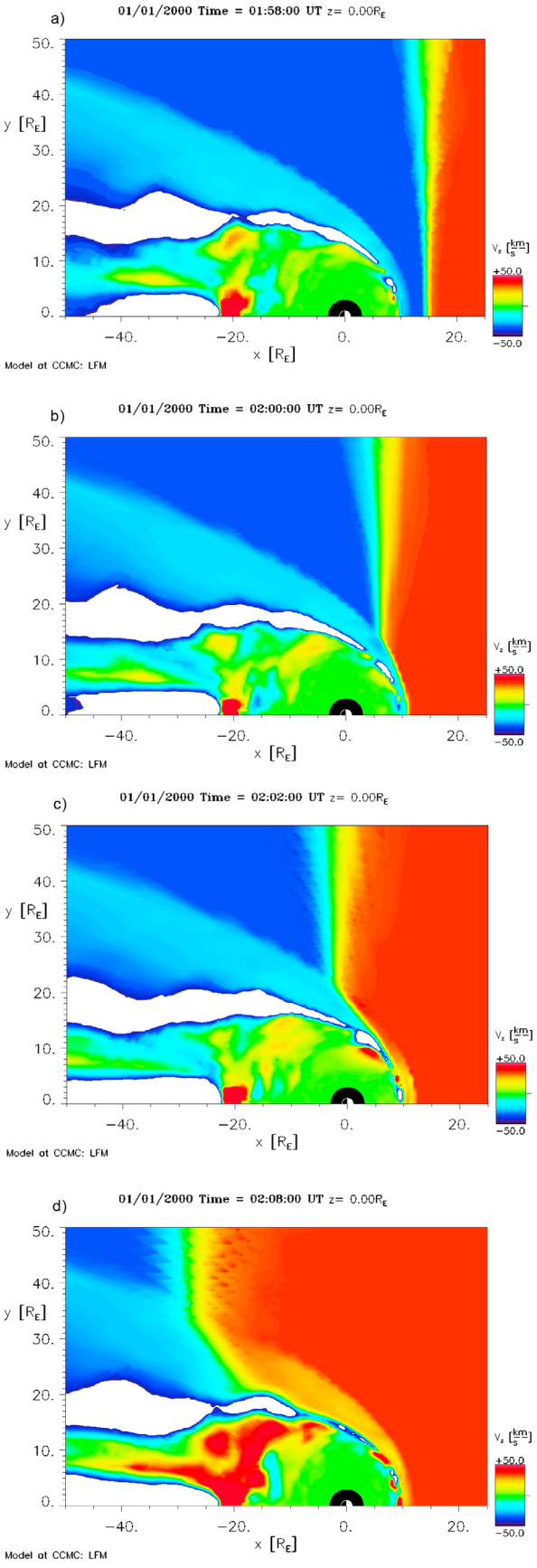

or downward out of the plane) in blue and v_z positive (northward, or upward out of the plane) in red. In Figure 7a the snapshot is taken just before the velocity shear reaches the Earth's bow shock at the nose. The shear layer is located at $X \approx 15\ R_E$; Earthward of the shear layer the solar wind has $v_z = -40$ km/s (blue) and sunward of the shear layer the solar wind has $v_z = +40$ km/s (red). The Earth's magnetosheath shows up in Figure 7a as the lighter-blue plasma between the dark-blue solar wind and the differently colored magnetosphere. In Figure 7b the shear layer in the solar wind is located at $X \approx +6\ R_E$. At this time the shear layer has passed the nose of the bow shock and the shear layer can be seen entering the magnetosheath at the nose, but it has not reached the magnetopause. The advection velocity in the magnetosheath is slower than it is in the solar wind; at the nose the velocity v_x drops by a factor of 4 across the high-Mach-number bow shock and then continues to further decrease monotonically between the bow shock and the magnetopause [cf. *Borovsky et al.*, 2008, Figure 5]. In Figure 7c the velocity shear layer is located at $X \approx -2\ R_E$ in the solar wind. At this time the delay of the advection of the shear layer in the magnetosheath is clearly seen: at the nose the magnetosheath is yellow (northward flow) and at the terminator the magnetosheath is blue (southward flow) and the transition from southward flow to northward flow forms a curve inside of the magnetosheath. In Figure 7d the velocity shear in the solar wind is located at $X \approx -27\ R_E$. The delayed position of the shear layer in the magnetosheath along the flank of the magnetotail is clearly seen is the diagonal blue-to-red transition connecting up to the shear layer in the unshocked solar wind. The velocity shear layer contacts the magnetopause at $X \approx -17\ R_E$, which is a delay of $10\ R_E$ from the position of the shear layer in the unshocked solar wind. At a solar wind x velocity of 450 km/s, this 10-R_E lag is a 140-s delay, which is a 2.3-min delay.

[35] In Figure 8 the movement of the velocity shear layer through the magnetosheath along the *x* axis (nose cut), *y* axis (dusk terminator cut), and *z* axis (northward terminator cut) is shown from top to bottom, respectively. The various colored curves plotted are the plasma flow velocity v_z as a function of distance from the Earth, each curve at a different time. For each curve the position of the shear layer is denoted with a large circle on the curve. All measurements are taken from an LFM simulation (the same run as used in Figure 7) with the solar wind parameters of Table 3. Time $t = 0$ is taken as the time at which the velocity shear in the solar wind makes contact with the Earth's bow shock at the nose (on the *x* axis). Figure 8 (top) shows snapshots of v_z plotted along the *x* axis. The position of the bow shock ($X \approx 12\ R_E$) and the magnetopause ($X \approx 10\ R_E$) are indicated with the vertical dashed lines. The dark red curve at time $t = -1$ min shows the velocity shear layer in the solar wind upstream of the bow shock at $X \approx +15\ R_E$. Note the thickness of the

Figure 7. As a north-south velocity shear passes the Earth, the v_z plasma flow velocity is plotted in color for four snapshots of the equatorial plane. Red is upward flow ($v_z > 0$) and blue is downward flow ($v_z < 0$). Taking $t = 0$ to be the time when the shear layer contacts the bow shock at the nose, the time in the four snapshots are −0.5 min, 1.5 min, 3.5 min, and 9.5 min.

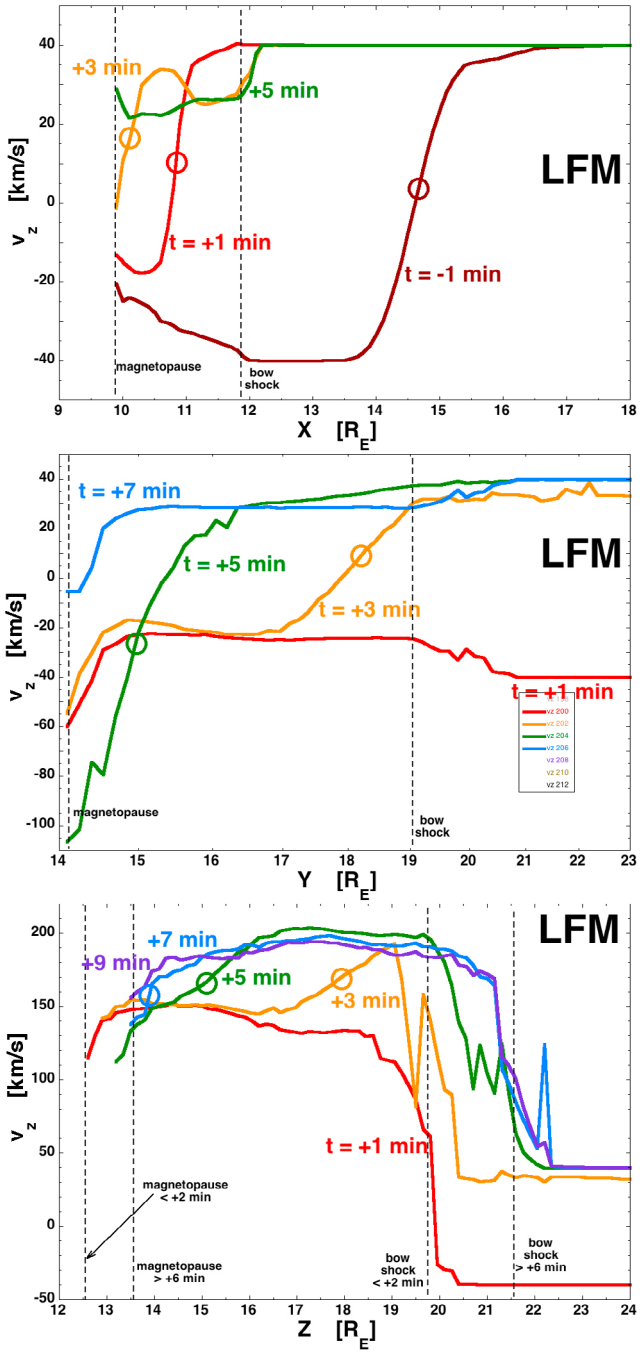

Figure 8. The plasma flow velocity v_z is plotted as functions of distance from the Earth at several snapshots of time. (top) Here v_z is plotted along the $+x$ axis (Earth-Sun line), (middle) v_z is plotted along the $+y$ axis (dusk terminator), and (bottom) v_z is plotted along the +Z axis (northward terminator). Circles on the curves mark the position of the north-south velocity shear.

shear layer in the solar wind is about 1 R_E. The red curve at t = +1 min shows the shear layer inside the magnetosheath at X ≈ 11 R_E and the yellow curve at t = +3 min shows the shear layer inside the magnetosheath near X = 10 R_E. The green curve at t = +5 min is past the time wherein the shear layer is advecting along the x axis. The velocity shear took more than 3 min to advect across the 2-R_E-thick magnetosheath from the bow shock to the magnetosphere. The mean speed for this was less than 50 km/s, which is less than 1/6 of the solar wind speed.

[36] Figure 8 (middle) shows snapshots of v_z plotted along the y axis (dusk terminator). The position of the bow shock (Y ≈ 19 R_E) and the magnetopause (X ≈ 14 R_E) at the terminator are indicated with the vertical dashed lines. The earliest curve shown in Figure 8 (middle) is the red curve at t = −1 min; at this time the velocity shear in the solar wind has not yet reached the dusk terminator. The yellow curve at time t = +3 min shows the velocity shear in the outer magnetosheath at Y ≈ 18 R_E just inside of the bow shock. The green curve at t = +5 min shows the velocity shear at Y ≈ 15 R_E, near the magnetopause. The blue curve at t = +7 min shows the v_z flow after the shear layer has completely passed the Y terminator: the spatial drop in v_z against the magnetopause is a permanent feature after time t = +7 min. On the order of 3 min is required for the flow shear to advect through the magnetosheath before reaching the magnetopause as seen from the dusk terminator. Note in Figure 8 (middle) that the plasma z-component flow stays negative at the magnetopause at the dusk terminator: this is because of the strong B_y in the solar wind leading to a dayside reconnection flow that has a downward (negative-z) component on the duskside and an upward component on the dawnside.

[37] Figure 8 (bottom) plots v_z along the Z axis (northern terminator). The plots are more complicated owing to (1) the strong v_z flow in the magnetosheath of shocked solar wind flowing up over the magnetosphere and (2) the fact that the position of the bow shock and magnetopause shift in reaction to the shifting windsock angle of the solar wind. In the magnetosheath (say at Z = 17 R_E) the magnetosheath flow will make a transition from v_z ≈ +100 km/s (red curve) to v_z ≈ +190 km/s (green, blue, and purple curves). The position of that transition in the magnetosheath is marked at three instants of time by the large circles on the yellow (t = +3 min), green (t = +5 min), and blue (t = +7 min) curves. Thus, the wind shear layer spends about 4 min in the magnetosheath before reaching the magnetopause as seen along the northern terminator.

4.2. Movement of the Bow Shock and the Magnetopause

[38] In Figure 8 (bottom) the z component of the plasma flow v_z is plotted along the Z axis (northern terminator) at several instances of time. Time t = 0 is the time at which the flow shear in the solar wind makes contact with the bow shock along the Sun-Earth axis. Out in the unshocked solar wind beyond Z ≈ 22 R_E the transition in the v_z flow in the solar wind from v_z = −40 km/s (red curve) to v_z = +40 km/s (green, blue, and purple curves) is seen in Figure 8 (bottom). In the simulation, the position of the Earth's bow shock can be easily discerned by a jump in the specific entropy of the plasma; the position of the bow shock for times t ≤ 2 min at X ≈ 19.8 R_E and the position of the bow shock for times t ≥ 6 min at X ≈ 21.5 R_E are marked by two vertical dashed lines. In the simulation, the position of the Earth's magnetopause can be easily discerned by a jump in the specific entropy of the plasma or by a rapid change in the x component of the magnetic field; the position of the magnetopause

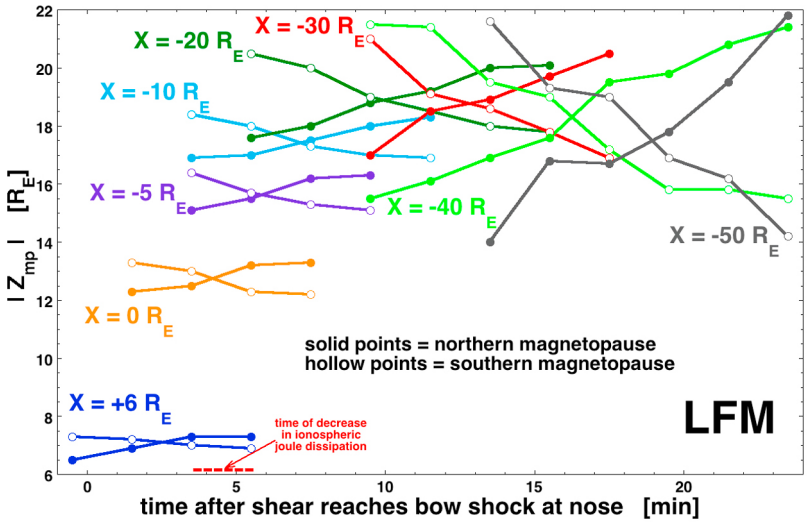

Figure 9. At various locations is X (various colors) the |Z| position of the northern (solid points) and southern (hollow points) magnetopause is plotted as a function of the time after a north-south velocity shear encounters the bow shock at the nose. The positions are only plotted near the times when the magnetopause position moves.

for times $t \leq 2$ min at $X \approx 12.5\ R_E$ and the position of the magnetopause for times $t \geq 6$ min at $X \approx 13.5\ R_E$ are marked by two vertical dashed lines.

[39] Owing to the change in the wind direction approaching the Earth, the position of the orientation of the quasi-parabolic bow shock shifts. The windsock angle changes by 10.2° as the solar wind with $v_x = -450$ km/s shifts from $v_z = -40$ km/s to $v_z = +40$ km/s. Along the Z axis, this shows up as a shift in the position of the bow shock from $X \approx 19.8\ R_E$ to $X \approx 21.5\ R_E$, which is a shift of about $1.7\ R_E$.

[40] Along with the change in the wind direction approaching the Earth, the location of the magnetopause also shifts. This is owed to a change in the force vector of the solar wind ram pressure on the magnetosphere. As can be seen in Figure 8, along the Z axis, this shows up as a movement in the magnetopause position from $X \approx 12.5\ R_E$ to $X \approx 13.5\ R_E$, which is a movement of about $1.0\ R_E$. At the northern terminator his movement occurs in less than 4 min, which is a motion of greater than 1500 km/min, which is greater than 26 km/s.

[41] Note in Figure 8 (top, dark red curve) that the thickness of the velocity shear layer in the solar wind is slightly greater than $1\ R_E$ in the simulation. At a solar wind flow velocity v_x of -450 km/sec, the shear is advected past a point in about 15 s. The movement of the magnetopause occurred over a timescale much larger than this 15-s passage time for the shear layer itself past a point. Hence, the timescale for the magnetopause motion was probably set by some flow-reorientation timescale for solar wind flow past the Earth, or by some global squeezing effect on the dipolar magnetosphere as the wind shear passes across it.

[42] In Figure 9 the Z motion of the northern and southern magnetopauses is tracked at various locations from $6\ R_E$ sunward of the terminator to $50\ R_E$ downtail in the LFM simulation with the solar wind parameters of Table 3. The magnetopause is located by a local maximum in the current density in the plasma. Every two minutes the Z position of the northern magnetopause and of the southern magnetopause is recorded. At various positions in X (colors) the absolute value of the Z position is plotted in Figure 9 around the times that the magnetopause moves. The Z position of the northern magnetopause is plotted with solid points and the $-Z$ position of the southern magnetopause is plotted with hollow points. Note the symmetry in the motion of the northern and southern magnetopauses: there is no apparent

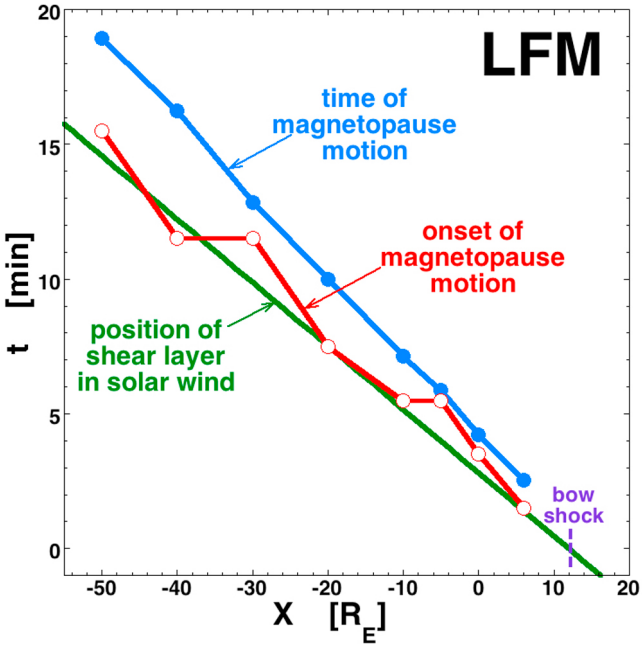

Figure 10. For the north-south-shear simulation of Figure 9, the time of major motion of the northern and southern magnetopause is plotted in blue as a function of X (downtail position) and the time of onset of the magnetopause motion is plotted in red. The X position of the shear layer as a function of time is plotted in green.

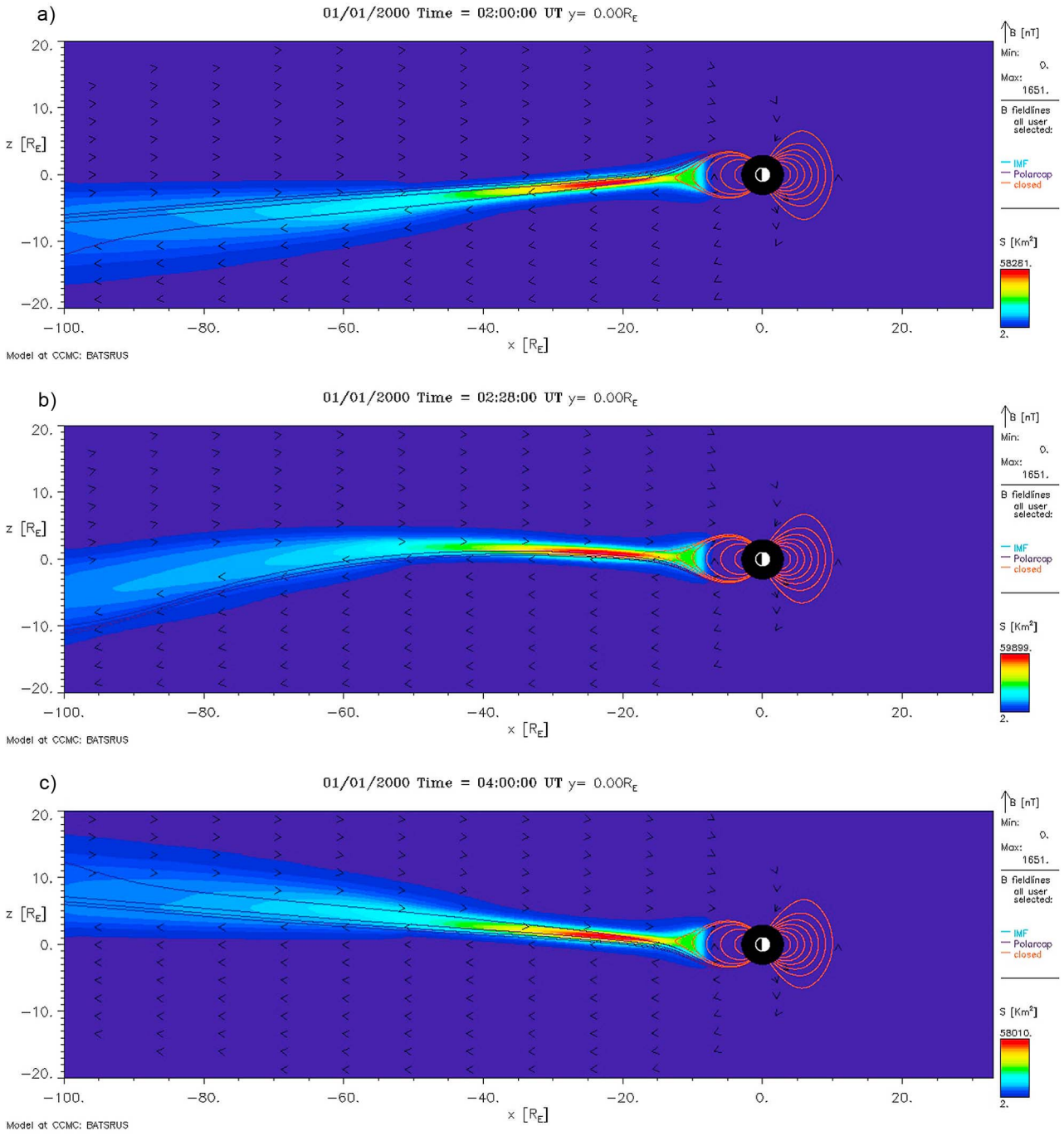

Figure 11. From at BATSRUS MHD simulation of a north-south velocity shear in the solar wind, the specific entropy of the plasma is plotted in color at three instants of time: (a) before the wind shear arrives, (b) as the wind shear passes through the simulation domain, and (c) after the wind shear has passed.

time lag for windward (southern) or leeward (northern) magnetopause motion when the wind direction shifts. Note that the time of magnetopause motion is later for positions further downtail (as expected). Note also that the amplitude of the position change is greater further downtail (as expected).

[43] In Figure 10 the timing of the magnetopause motion determined from Figure 9 is tracked. At each X location in Figure 10, two times are plotted. The first time is the central time for the magnetopause motion, taken as the time at which the northern and southern curves cross for each downtail position in Figure 9. The second time is the time at which the magnetopause begins its motion in the curves of Figure 9, denoted the onset time; this is the second point plotted for each pair of differently colored curves in Figure 9. In Figure 10 the central time of the motion is plotted in blue and the onset time is plotted in red. Plotted in green in Figure 10 is the X(t) trajectory of the shear layer in the unshocked solar

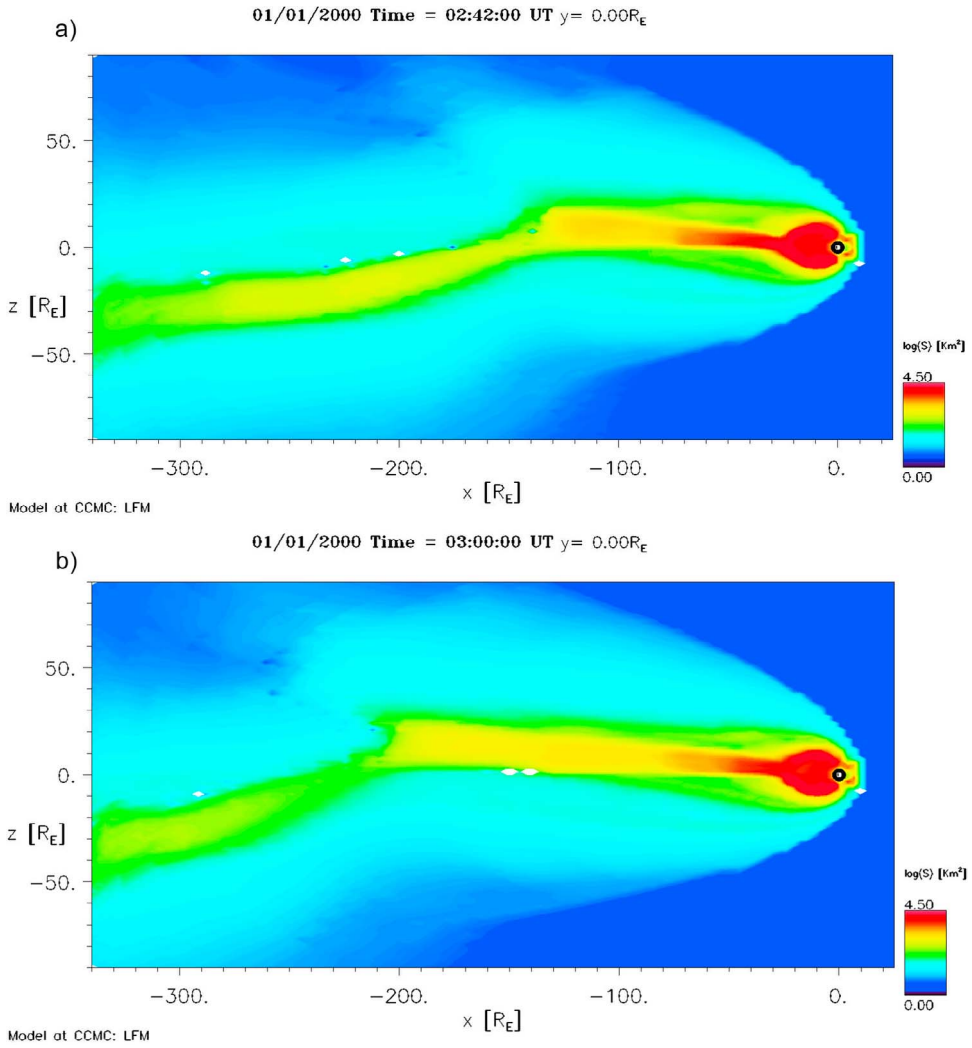

Figure 12. From an LFM MHD simulation of the reaction of the magnetosphere to a north-south wind shear, the logarithm of the specific entropy is shown at two instants of time: (a) 43.5 min and (b) 61.5 min after velocity shear first contacts the bow shock.

wind, with t = 0 as the time the shock reaches the nose of the bow shock at X = +12 R_E. Note in Figure 10 that the onset time for magnetopause motion (red) is approximately the time of passage of the shear layer in the solar wind (green). There is no time lag, despite the fact that the shear layer itself has a lag of 3 or 4 min for propagation through the magnetosheath to make contact with the magnetopause (see section 4.1). As can be seen in Figure 10, the central time of magnetopause movement lags the passage of the shear layer and that the amount of time lag increases with downtail distance.

4.3. Re-orientation and Disconnection of the Earth's Magnetotail

[44] As a velocity shear passes the Earth, the direction vector of the solar wind flow velocity changes. This results in a change of the "windsock" angle of the solar wind, which must result in a change in the orientation of the magnetotail with respect to the Earth-Sun line [cf. *Hones et al.*, 1986; *Fairfield*, 1993; *Owen et al.*, 1995]. In Table 2 it is noted that a typical change in the windsock angle is 6.7° for the collection of $\Delta v > 60$ km/s wind shears.

[45] In Figure 11 three views of the Earth's magnetotail are shown from a BATSRUS simulation with a north-south wind shear of $\Delta v_z = 80$ km/s. The solar wind conditions for the simulation are listed in Table 3. The quantity plotted in color in Figures 11a–11c is the logarithm of the plasma specific entropy $S = T/n^{2/3}$, which highlights the high-specific-entropy plasma sheet in the magnetotail. In Figure 11a the orientation of the tail is shown when $v_z = -40$ km/s in the solar wind prior to the arrival of the wind shear. In Figure 11c the orientation of the tail is shown when $v_z = +40$ km/s in the solar wind long after the shear has passed. In Figure 11b the magnetotail is shown when the shear layer is located at X = −97 R_E downtail from the Earth. In Figure 11 the magnetotail shows a bend making the necessary transition from a downward-tilted tail ahead of the velocity shear to an upward-tilted tail behind the shear.

[46] Further downtail the transition in tail orientation is not so smooth. In Figure 12 two snapshots of the Earth's

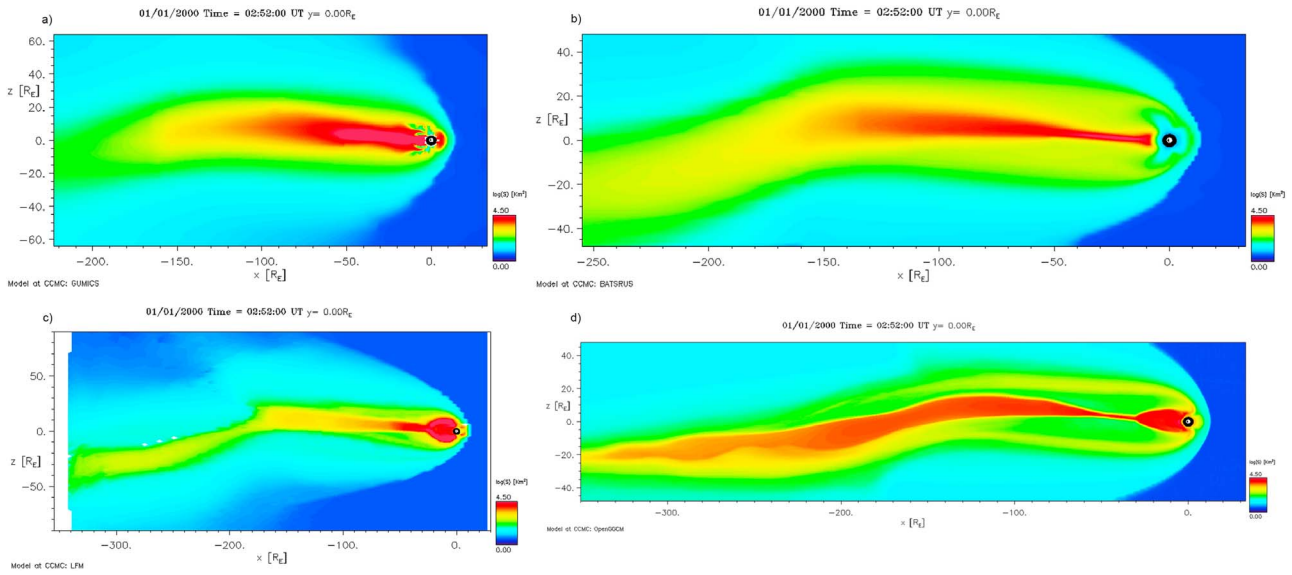

Figure 13. With the same solar wind conditions, the logarithm of the specific entropy of the magnetosphere at Y = 0 is plotted at time t = 2:52 simulated with four different codes with four different simulation-domain sizes. The codes are (a) GUMICS, (b) BATSRUS, (c) LFM, and (d) OpenGGCM.

magnetotail are shown from an LFM simulation with the standard solar wind parameters of Table 3. At the time of the top snapshot the solar wind velocity shear is located at X = −173 R_E and at the time of the bottom snapshot it is at X = −249 R_E. Earthward of this shear the solar wind has v_z = +40 km/s and downtail from this shear the solar wind has v_z = −40 km/s. The color coding in Figure 12 is the logarithm of the plasma specific entropy S, showing the high-specific-entropy plasma sheet plasma. As can be seen, in the distant tail the transition from downward-orientation to upward orientation is more abrupt.

[47] This abrupt transition further downtail is seen in all four of the simulation codes used. In Figure 13 snapshots of the magnetosphere from the four codes at the same time are shown. The logarithm of the plasma specific entropy in the Y = 0 plane is plotted. Note the different sizes of the X-Z simulation domains for the four codes. As can be seen, all show an abrupt transition downtail. Note, however, that the domain of the LFM code is the largest in the z direction (it is a cylinder with radius 125 R_E) so it has the most room for the magnetotail to swing without hitting a boundary and it has the largest reservoir of solar wind around the magnetotail.

[48] In Figure 14 some north-south motions of magnetotail features are tracked as functions of time as the wind shear passes the Earth. In Figure 14 (top) the Z position of the magnetotail neutral sheet at X = −20 R_E is plotted (hollow points) and the Z position of the magnetotail neutral sheet at X = −60 R_E is plotted (solid points). The four colors represent measurements extracted from four different simulations: red pertains to Open-GGCM, green pertains to BATSRUS, orange pertains to GUMICS, and blue pertains to LFM. All four simulations were run with the standard solar wind parameters of Table 3. At the bottom of the plot the times at which the velocity shear in the solar wind passed the Earth, passed X = −20 R_E, and passed X = −60 R_E are noted. Looking at the hollow-point curves for X = −20 R_E in Figure 14 (top) it is seen that the down-to-up transition of the neutral sheet is from about Z = −0.8 R_E to about Z = +1 R_E in about 20 min. This corresponds to a speed of about 10 km/s upward (v_z positive). Looking at the solid-point curves for X = −60 R_E in Figure 14 (top) it is seen that the down-to-up transition of the neutral sheet is from about Z = −4.5 R_E to about Z = +5 R_E in 20 min. This corresponds to a speed of about 50 km/s upward (v_z positive). These motions are greater further downtail. In Figure 14 (bottom) at X = −200 R_E the solid-square points plot the z position of the B_x maximum location in the magnetotail. (In the distant magnetotail with a solar wind B_y, the twist of the magnetotail [cf. *Sibeck et al.*, 1985; *Maezawa et al.*, 1997] makes locating the Z position of the neutral sheet difficult owing to the near-vertical orientation of the neutral sheet: instead the Z position of the B_x = maximum point is taken.) The z transition of this maximum is from Z = −15 R_E to Z = +25 R_E in 28 min. This corresponds to an upward velocity of 150 km/s. Note that this 150 km/s is much faster than the ∼50 km/s Alfven speed in the magnetotail at X = −200 R_E. Examining plasma flows in the simulation, no z-direction flows anywhere near the speed of 150 km/s are found: at X = −200 R_E the maximum v_z values for the plasma are less than 60 km/s.

[49] Two sketches pertaining to the re-orientation of the magnetotail appear in Figure 15. In the top sketch two positions of the magnetotail are drawn: the old downward position long before the shear reaches the Earth and the new upward position long after the shear passes. As the velocity shear layer passes the Earth and magnetotail, the magnetotail will make a transition from the downward position to the upward position. For the near-Earth portion of the magnetotail this transition occurs at low speeds (see Figure 14, top) and the bend in the tail will be mild (see Figure 11). However, further down the tail the vertical transition distance from the downward position to the upward position is larger and the transition speeds will be larger (see Figure 14,

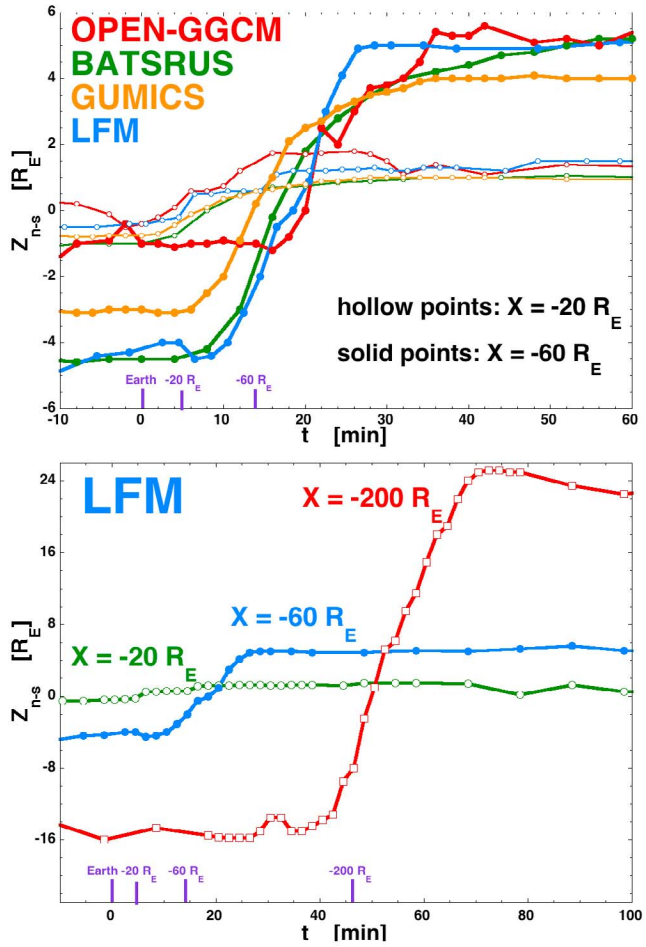

Figure 14. (top) For four MHD simulations (colors), the Z position of the magnetotail neutral sheet is plotted as a function of time at X = −20 R_E (hollow points) and at X = −60 R_E (solid points). (bottom) For a single simulation with the LFM code, the Z position of the neutral sheet is plotted at X = −20 R_E (green) and at X = −60 R_E (blue) and the Z position of the maximum-B_x location in the magnetotail is plotted at X = −200 R_E. In both panels the horizontal axis is the time since the velocity shear was located at X = 0.

bottom). Eventually the transition speeds will become superAlfvenic for the Alfven speed of the plasma in the magnetotail. Then the situation will occur that is sketched in Figure 15 (bottom). Here the velocity shear in the solar wind is depicted as the boundary between the downward-moving blue block of plasma and the upward-moving pink block of plasma. Ahead of the wind shear (to the left) the old downward-oriented magnetotail is drawn; since the wind shear layer is moving with the solar wind speed, which is greater than the Alfven speed in the magnetotail, this portion of the old magnetotail has no warning about the approaching wind shear. In the wind shear interface, magnetotail material is trapped and is sheared into a vertical remnant magnetotail with remnant magnetic field structure from the magnetotail and with high-specific-entropy magnetospheric plasma. Within the distant magnetotail, magnetotail plasma flows antisunward faster and faster the further from Earth [*Slavin et al.*, 1985; *Paterson and Frank*, 1994]. Behind the shear layer (to the right in Figure 15) a new magnetotail is being drawn outward in the upward-oriented position by the solar wind.

[50] To examine the tail-disconnection further and to analyze the remnant magnetotail in the shear, two additional simulations are run with the LFM computer code. The simulation parameters differ from those in Table 3 in that the solar wind speed is v_x = −300 km/s (instead of −450 km/s) and the wind shear is ±50 km/s (instead of ±40 km/). One run has the wind shear in v_z (north-south shear) and the other run has the wind shear in v_y (east-west shear). In Figure 16 the remnant magnetotail is analyzed for the LFM run with the v_z = ±50 km/s shear. In the figure the position of the remnant magnetotail is drawn at instants of time 10 min apart: each position at a different time is drawn in a different color. The times labeled are the times from the encounter of the wind shear with the nose of the bow shock at X = +14 R_E. The positions of the old (prior to the shear) and the new (after the shear) magnetotails are indicated with gray dashed curves in Figure 16. The positions of the wind shear layer in the solar wind every 10 min are

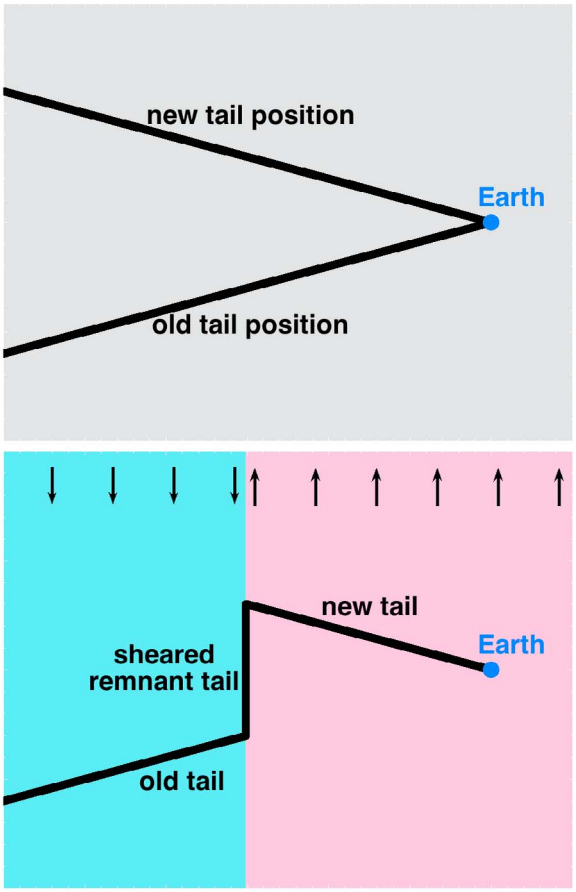

Figure 15. (top) A sketch depicting the "old" and "new" orientations of the magnetotail before and after a velocity shear passes. (bottom) A sketch of a snapshot of the old and new tails as the shear is passing, emphasizing the remnant of the magnetotail that is caught up in the solar wind shear layer.

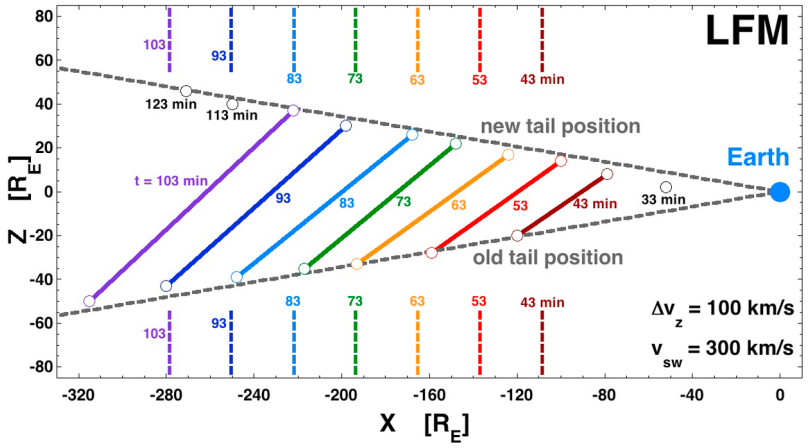

Figure 16. From an LFM MHD simulation with a north-south velocity shear, the position and orientation of the remnant magnetotail is drawn (solid color lines) every 10 min as the magnetotail goes through a disconnection. The dashed color lines are the position of the shear layer in the solar wind every 10 min. The labeled times are the times after the shear layer encounters the nose of the bow shock.

marked with the vertical dashed lines across the top and bottom of the sketch, labeled according to the time, with colors matching the time of the remainder-tail measurements. The remnant magnetotail forms a bar that connects the sunward end of the old tail with the anti-sunward end of the new tail (e.g., Figure 12). (Compare Figure 16 with *Hones et al.* [1986, Figure 2].) As can be seen, the bar moves downtail at about the solar wind x velocity of 300 km/s (18.4 R_E per 10 min). Note that each bar is centered in X position at about the X value of the shear layer in the solar wind. In Figure 17 the length of the bar is plotted as a function of time for the 7 snapshots of the bar in Figure 16. A linear-regression fit in Figure 17 to the length L of the bar versus time t yields an expansion speed dL/dt of 1.16 R_E/min, which is 123 km/s. At time t = 88 min the magnetic field strength and plasma number density are examined for an X = −240 R_E slice through the remnant magnetotail to estimate the Alfven speed in the remnant. The fastest Alfven speed found was $v_A \sim 65$ km/s, corresponding to B ∼ 5 nT and n ∼ 3 cm^{-3}. Hence, the bar is lengthening at about twice the Alfven speed. Causality for dynamical (electromotive) interactions in a large-scale (MHD) magnetized plasma is governed by the Alfven speed v_A along the magnetic field [*Drell et al.*, 1965; *Goertz and Boswell*, 1979], meaning that the two ends of the bar are not causally connected. The examination of the X = −240 R_E slice finds the temperature to be ∼50 eV in the magnetotail remnant, yielding a magnetosonic speed of about 90 km/s; hence the bar is lengthening at supersonic speed. Hence the old tail is disconnected from the new tail and the remnant magnetotail is plasma from the tail that is captured in the solar wind shear. The presence of the old tail has no influence on the new tail.

[51] This is further demonstrated in Figure 18 from the LFM simulation analyzed in Figures 16 and 17. Figures 18a and 18b are Y = 0 R_E slices of the magnetotail again at time t = 88 min (measured from the time that the wind shear contacts the bow shock). In Figure 18a the logarithm of the specific entropy S is plotted in color. The red and yellow regions are the high-entropy plasma sheet plasma. The new, upward-oriented magnetotail is visible to the right of X ∼ −210 R_E and the old, downward-oriented magnetotail is visible to the left of X ∼ −290 R_E; the remnant magnetotail is seen forming a bar that connects the two tails. In Figure 18b the v_z velocity of the plasma is shown at the same time in the same slice. Blue colors are $v_z < 0$ plasma moving downward and yellow and red colors are $v_z > 0$ plasma moving upward. As can be seen by comparing Figures 18a and 18b, the shear from the solar wind is running right through the magnetotail with little impediment to the flow pattern. With time it pulls the old and new magnetotails further and further apart at a speed exceeding the Alfven speed of the magnetotail plasma.

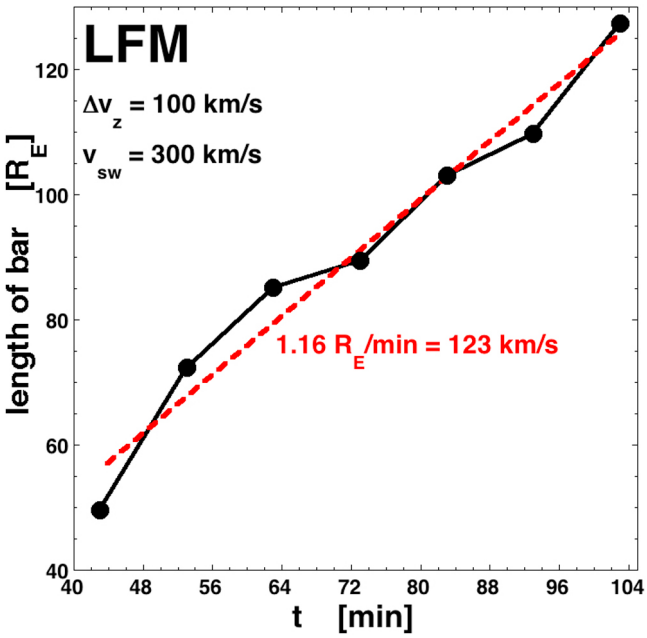

Figure 17. For the 7 measurements of the remnant magnetotail in Figure 16, the length of the remnant magnetotail is plotted as a function of time (black points) and a linear-regression fit is shown in red.

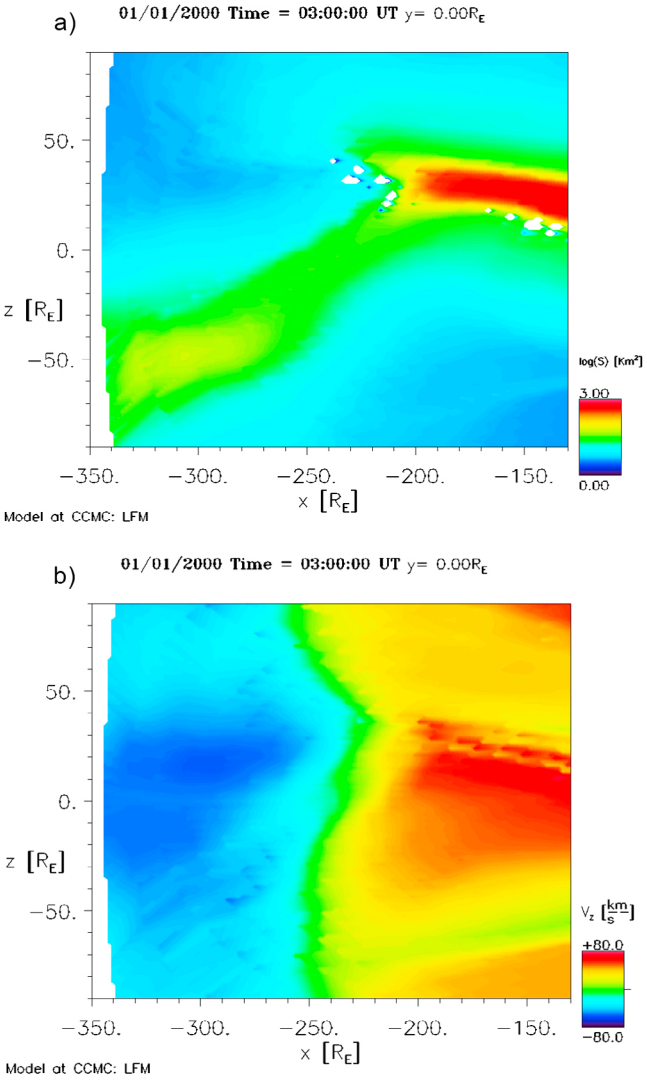

Figure 18. During a magnetotail disconnection, the logarithm of the (a) specific entropy and (b) plasma v_z flow velocity are plotted for a Y = 0 cut spanning the remnant magnetotail. The shearing of the entire tail is seen.

[52] Another view of magnetotail disconnection produced by sudden wind shear appears in Figures 19 and 20. In this LFM simulation an east-west wind shear in the solar wind encounters the Earth. The solar wind parameters are the same as those for the simulation of Figures 16–18, except the shear is $v_y = \pm 50$ km/sec and $v_z = 0$ (with $v_x = -300$ km/s). In Figures 19a–19d the plasma number density is shown in color in the Z = 0 plane (equatorial plane). In Figure 19a the shear layer is located at X = 4.3 R_E, just upstream of the Earth's position. The yellow-red parabola is the high-density portion of the magnetosheath behind the bow shock and the dark blue area is the magnetotail. The tail is seen oriented in the −Y direction with $v_y = -50$ km/s in the wind. In Figure 19b the shear layer is located at X = −36 R_E in the solar wind. The distortion of the magnetosheath at 20–40 R_E behind the Earth is clearly seen. In Figure 19c the shear layer is located at X = −81 R_E in the solar wind: at this time a disconnection of the magnetosheath is seen on the dusk flank at X ∼ 80 R_E. The sideways distortion of the

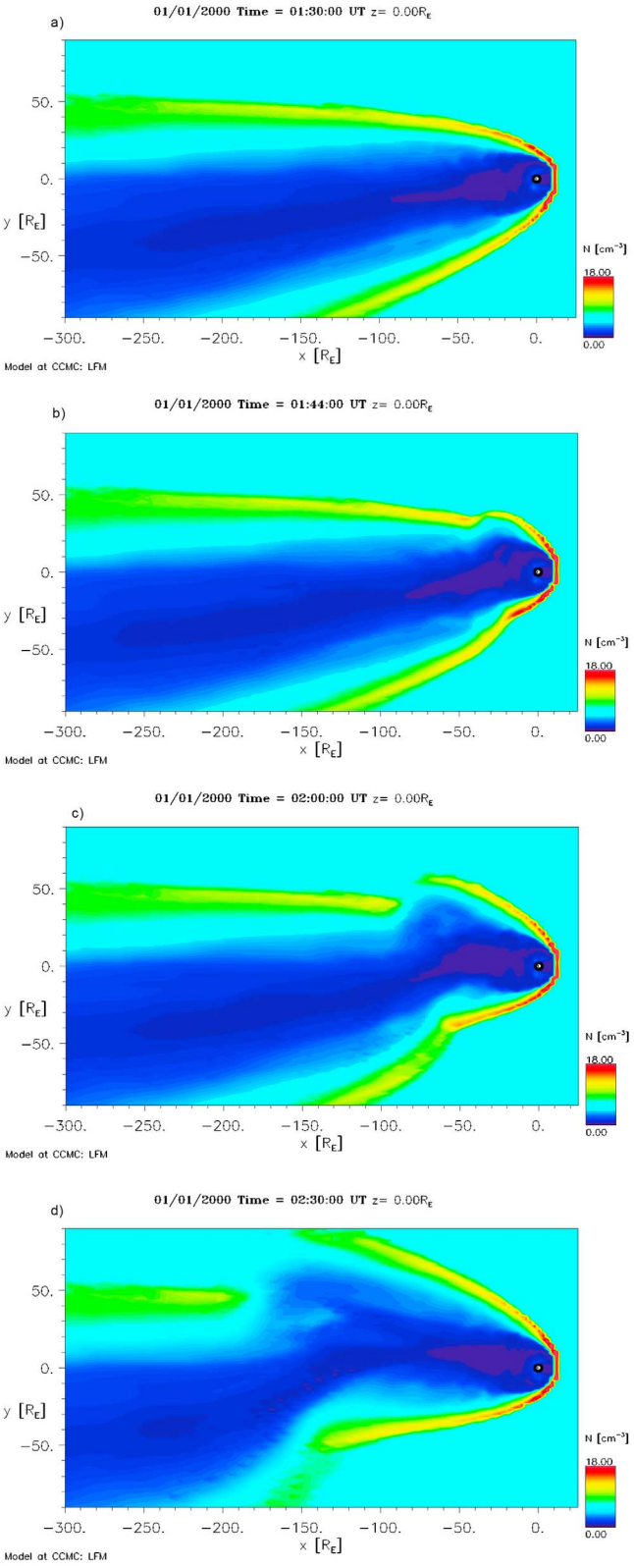

Figure 19. For an east-west velocity shear the plasma number density is plotted in the equatorial plane at four instants of time. (a–d) The velocity shear is located at X = +4 R_E, −36 R_E, −81 R_E, and −166 R_E. The disconnection of the magnetosheath (yellow region) is seen.

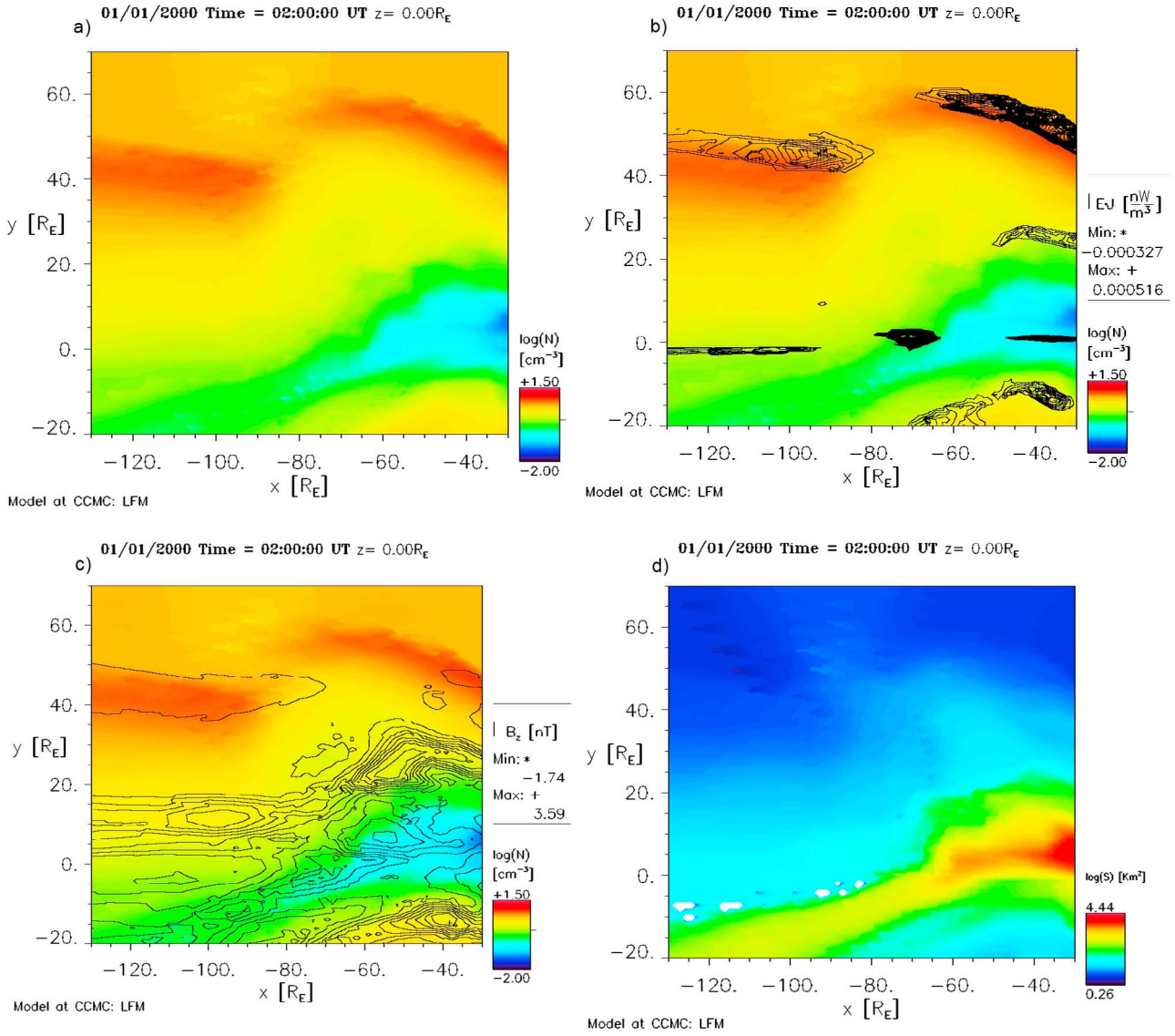

Figure 20. The magnetotail disconnection for an LFM simulation with an east-west shear is examined in detail with simultaneous cuts in the equatorial plane. (a) The logarithm of the plasma number density is plotted in color, (b) a black contour plot of the Ohmic dissipation is overlaid on the number density, (c) a black contour plot of the z component of the magnetic field is overlaid, and (d) the logarithm of the plasma specific entropy is plotted in color.

magnetotail (dark blue) is also seen. In Figure 19d the shear layer is located at X = −166 R_E. Here a clear disconnection of the magnetosheath on both sides of the magnetotail is seen in the 150–180 R_E downtail region. The strong sideways distortion of the magnetotail (dark blue) is also seen, reminiscent of the distortion seen in the north-south-shear simulation of Figure 12.

[53] In Figure 20 the disconnection of the magnetosheath is examined in further detail. Here various quantities are plotted in the Z = 0 plane at a time when the shear layer is located at X = −81 R_E (same time as Figure 19c). In Figure 20a the logarithm of the plasma number density is plotted. The high-density portion of the magnetosheath appears in reddish-orange. Note these magnetosheath regions are clearly disconnected by the wind shear. In Figure 20b the logarithm of the number density is replotted in color and a contour plot of −j•E is overplotted in black. The black-highlighted areas on the edge of the reddish-orange regions is the bow shock along the magnetosheath at the magnetospheric flanks [cf. *Greenstadt et al.*, 1990; *Merka and Szabo*, 2004]: note in Figure 20b that the bow shock is clearly disconnected along with the magnetosheath. In Figure 20c the logarithm of the number density is replotted in color and a contour plot of B_z is overplotted in black. The region where the contours of B_z are plentiful is the magnetotail where plasma with northward B_z has been reconnected near the Earth and has been flowing downtail. Since $\underline{B} = (0, B_y, 0)$ in the solar wind, in the equatorial plane the solar wind and magnetosheath have $B_z \approx 0$. In Figure 20c, the gap between the region of $B_z \neq 0$ (region of black contours) and the high-density magnetosheath (reddish-orange bar-shaped regions) is a region of low-density magnetosheath. On the flanks of

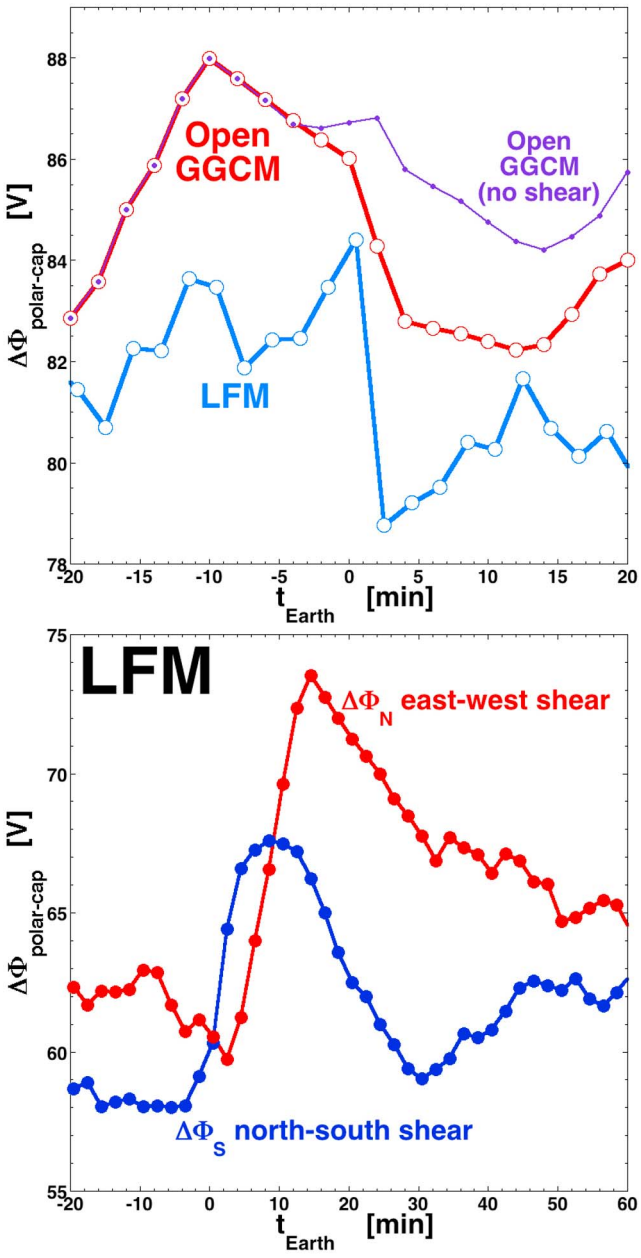

Figure 21. (top) The cross-polar-cap potentials for the northern polar cap are plotted for three simulations with north-south shears (see text for details). (bottom) The northern (red) and southern (blue) cross-polar-cap potentials for an east-west velocity shear (red) and a north-south velocity shear (blue).

the magnetosphere and down the tail, the magnetosheath has a wide low-density region near the magnetopause and a higher-density region just inside the bow shock [cf. *Steinberg and Lacombe*, 1992, Figures 3 and 4], with the density in the low-density region being less than the density of the unperturbed solar wind and the density of the high-density region being greater than the density of the solar wind [cf. *Spreiter et al.*, 1966, Figures 6 and 10]. In Figure 20d the logarithm of the specific entropy is plotted in color. The yellow high-entropy region is plasma sheet plasma in the center of the plasma sheet. Examining Figure 20, the dislocation of the magnetotail is clearly seen, the dislocation of the magnetosheath is clearly seen, and the dislocation of the bow shock is clearly seen.

4.4. Changes in the Ionospheric Potential

[54] In the MHD simulations of the solar wind-driven magnetosphere, sudden changes in the cross-polar-cap electric potential and in the total amount of ionospheric joule dissipation are seen at about the time the strong wind shear passes the Earth. In Figure 21 (top) the cross-polar-cap potential $\Delta\Phi$ for the northern polar cap is plotted as a function of time from three simulations. The red hollow points and the blue hollow points are from an Open-GGCM and an LFM simulation using the solar wind parameters of Table 3 with shears in Δv_z ($=\pm 40$ km/s). Time t = 0 is when the velocity shear layer in the solar wind passes the Earth (X = 0). As can be seen in Figure 21 (top), both simulations show a drop in the northern polar-cap potential just after time t = 0. (Both simulations show simultaneous increase in the southern polar-cap potential, not shown.) The purple curve in Figure 21 (top) is the northern polar-cap potential for an Open-GGCM simulation with identical initial solar wind conditions but without the wind shear; a comparison of the two Open-GGCM curves indicates that the drop in the polar-cap potential after t = 0 is attributable to the velocity shear passing the Earth.

[55] In Figure 21 (bottom) the cross-polar-cap electrical potential $\Delta\Phi$ is plotted as a function of time from two other LFM magnetospheric simulations. These two simulations used the solar wind parameters of Table 3 except the solar wind speed v_x was reduced from -450 km/s to -300 km/s and the size of the shear was increased from ± 40 km/s to ± 50 km/s. The red curve has an east-west shear where v_y of the solar wind goes from $v_y = -50$ km/s to $v_y = +50$ km/s with $v_z = 0$ and the blue curve has a north-south shear where v_z goes from $v_z = -50$ km/s to $v_z = +50$ km/s with $v_y = 0$. The red curve plots the potential of the northern ionosphere (the hemisphere who's potential increases in the east-west simulation) and the blue curve plots the potential of the southern ionosphere (the hemisphere who's potential increases in the north-south simulation). Note the difference in the temporal profiles of the ionospheric potentials. For the north-south shear (blue curve) the potential begins its change a few minutes before time t = 0 just after the shear contacts the bow shock at the nose whereas for the east-west shear (red curve) the potential begins its change after t = 0 which is after the shear has passed the position of the Earth. This implies that dayside currents play a more-important role in the change of the polar-cap potential for the north-south shear than for the east-west shear. For the north-south shear (blue curve) the increase in the polar-cap potential reverses before t = 10 min whereas for the east-west shear (red curve) the increase in the potential reverses at about t = 15 min. This seems to indicate a more-dominant role of magnetotail currents for the change in the polar-cap potential for east-west shears than for north-south shears.

[56] For the LFM simulation with the $v_y = \pm 50$ km/s east-west shear, the reorientation of some ionospheric patterns are examined in Figure 22. In Figures 22a–22c the electrical potential pattern in the northern polar cap is plotted at three instants of time: 0.5 min prior to the shear reaching

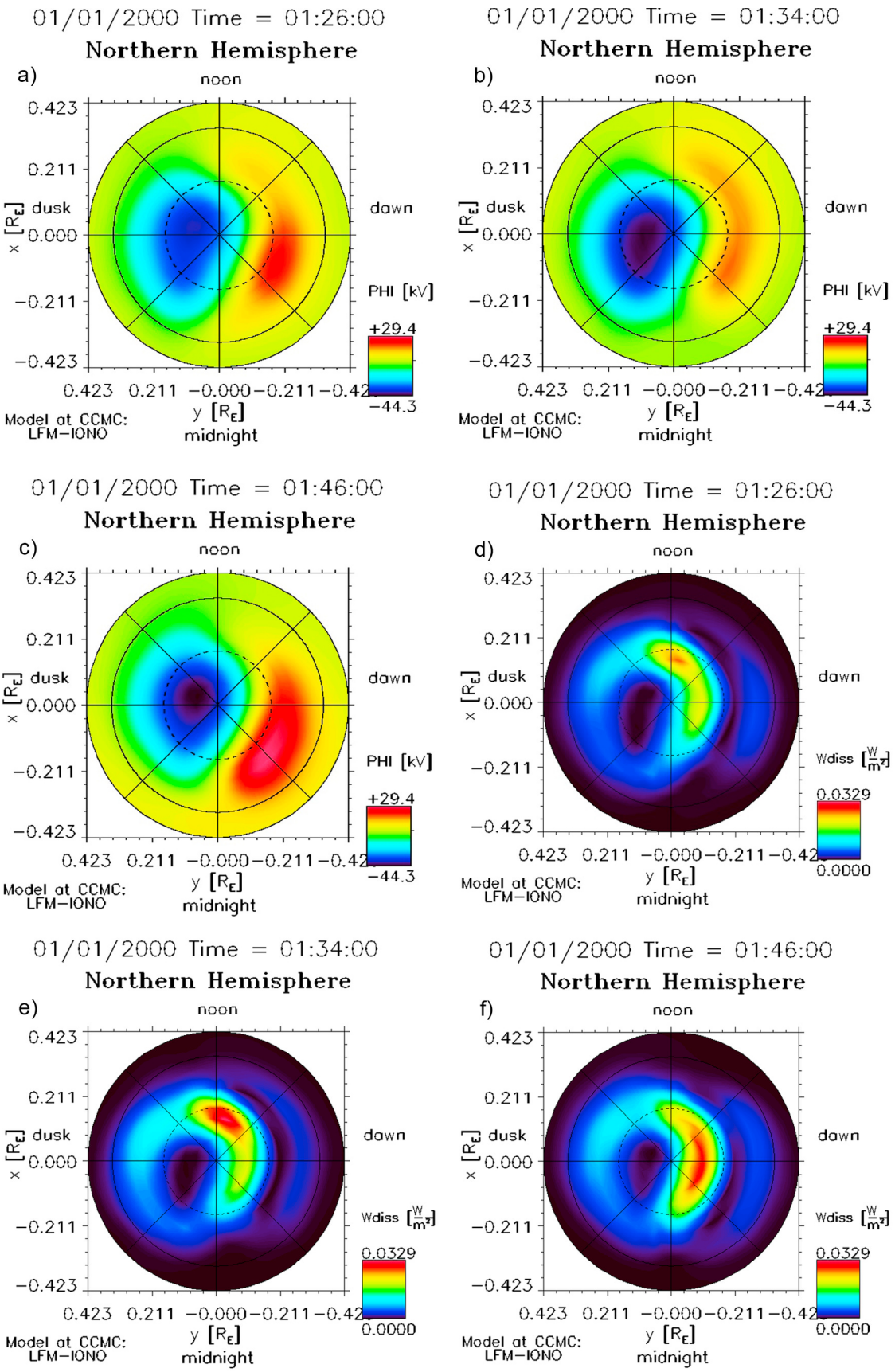
01/01/2000 Time = 01:26:00
Northern Hemisphere
a)
noon
dusk
dawn
midnight
x [R_E]
y [R_E]
0.423
0.211
0.000
−0.211
−0.423
PHI [kV]
+29.4
−44.3
Model at CCMC:
LFM−IONO
01/01/2000 Time = 01:34:00
Northern Hemisphere
b)
01/01/2000 Time = 01:46:00
Northern Hemisphere
c)
01/01/2000 Time = 01:26:00
Northern Hemisphere
d)
Wdiss [W/m³]
0.0329
0.0000
01/01/2000 Time = 01:34:00
Northern Hemisphere
e)
01/01/2000 Time = 01:46:00
Northern Hemisphere
f)

Figure 22

the bow shock, 7.5 min after the shear layer reaches the shock, and 19.5 min after the shear reaches the shock. In Figures 22d–22f the Joule dissipation in the ionosphere is plotted for the same three times. In Figures 22a and 22d the polar-cap-potential configuration is shown prior to the arrival of the shear with $v_y = -50$ km/s in the solar wind. In Figures 22b and 22e the shear layer is at $X = -7$ R_E; a shift of the potential pattern into the pre-noon sector of the ionosphere is clearly seen from the left-hand panel to the middle panel as the Joule dissipation in the noon sector increases. Between the middle panels and the right-hand panels clockwise rotations of the polar-cap potential pattern and the dissipation pattern are seen; during this time interval the shear layer moves from 7 R_E downtail to 41 R_E downtail. After the time of Figures 22c and 22e the potential patterns cease to rotate.

5. Discussion

[57] This section contains discussions about (a) the differences between the simplified shear layers that were used in the simulations and actual shear layers in the solar wind, (b) the possible effects that velocity shears could have on the Earth's magnetosphere-ionosphere system, (c) the analogy between the Earth's magnetotail's behavior and comet-plasma-tail behavior, (d) future simulations that are called for, and (e) future data analysis that is needed.

5.1. Sudden Wind Shears in the Solar Wind

[58] For the magnetotail simulations of section 4, the velocity shear layers in the solar wind are idealized. Actual shear layers will have some important differences.

[59] The orientation of the shear planes in the simulations of section 4 were all taken to be perpendicular to the radial direction, i.e., the normal vector to the plane is aligned with the Earth-Sun line. As seen in Figure 4 the normal to the velocity-shear layers in the solar wind can be in any direction, with a strong tendency for the normals to be perpendicular to the direction of the Parker spiral. In general the planes will be strongly inclined to the solar wind flow direction and will tend to slice through the magnetosphere at an oblique angle as they pass downstream.

[60] As discussed in sections 2 and 3, the velocity-shear layers of the solar wind also have magnetic field direction changes across them; the magnetic field vectors on both sides of the layer are both perpendicular to the normal of the layer.

[61] The velocity-shear layers of the solar wind are in general narrower than the shear layers in the simulations of section 4. The thicknesses of the shear layers in the simulations were limited by the grid resolution in the upstream solar wind and in the solar wind along the flanks of the magnetosphere. The shear layers in the simulation had thicknesses of 1 R_E or more; actual solar wind shear layers have thicknesses more like 0.5 R_E or less.

[62] Shear layers in the solar wind can be isolated in time, or shear layers can pass the Earth incessantly. As noted in Table 1, about 60 shear layers with $\Delta v > 50$ km/s pass the Earth per day in fast solar wind. That's an average of one shear layer every 24 min, and intervals of fast solar wind can last for several days.

5.2. Some Potential Effects on Earth of Sudden Velocity Shears

[63] One potential effect of the passage of a velocity-shear layer is the triggering of geomagnetic activity. In the last few decades there has been a focus on the question of whether or not sudden turnings of the solar wind magnetic field trigger the occurrence of magnetospheric substorms (see section 1.3). The possible role of the sudden velocity shear that accompanies the sudden magnetic turnings has not been considered in the investigations. North-south versus east-west shears may effect destabilization of the magnetotail differently [cf. *Kivelson and Hughes*, 1990] where it is argued that a magnetotail that is bent in the north-south direction is more unstable than a straight magnetotail). A preliminary study of the temporal association between strong vorticity events in the solar wind and the occurrence of substorm onsets using the Morley-Freeman technique [*Morley and Freeman*, 2007; *Freeman and Morley*, 2009] found no association (S. Morley, private communication, 2011).

[64] The passage of velocity-shear layers may excite ULF oscillations inside the magnetosphere. ULF oscillations are of particular interest for their potential role in energizing the outer electron radiation belt through drift-resonance interactions and through radial diffusion [*Elkington et al.*, 1999; *Shprits et al.*, 2008]. During long intervals of fast wind the electron radiation belt is energized in particular [*Paulikas and Blake*, 1979; *Reeves et al.*, 2011] and the levels of ULF magnetic field oscillations inside the magnetosphere is seen to be high during those intervals [*Anderson et al.*, 1990; *Sanny et al.*, 2007; *Borovsky and Denton*, 2010b]. This is also a time when the velocity shears in the solar wind are plentiful (cf. Table 1). The production of ULF oscillations in the magnetosphere from solar wind variations have been considered, but most analysis focuses on variations of the solar wind ram pressure (i.e., typically variations in the solar wind number density) [e.g., *Menk et al.*, 2003; *Takahashi and Ukhorskiy*, 2008; *Viall et al.*, 2009]. Variations in vector $\underline{v}$ of the solar wind have not been considered other than the wind speed variations that result in variations of the scalar ram pressure [e.g., *Liu et al.*, 2010; *Potapov and Polyushkina*, 2010]. The interaction of the velocity shear with the magnetosphere could lead to ULF oscillations in the magnetosphere. One manner is through the motion of the magnetopause (cf. Figures 8 and 9). Magnetopause motions associated with Kelvin-Helmholtz instabilities are often invoked to produce ULF fluctuations inside the magnetosphere [e.g., *Lee and Olson*, 1980; *Mathie and Mann*, 2000; *Pilipenko et al.*, 2010]. A second manner through which ULF might be produced is through the changing internal currents of the magnetosphere as a result of

Figure 22. The intensification and rotation of (a–c) polar-cap potential pattern and (d–f) the joule-dissipation pattern for an LFM simulation with an east-west velocity shear. Snapshots in Figures 22a and 22d are taken 0.5 min before the shear layer encounters the bow shock when the shear layer is at $X = 15.5$ R_E, snapshots in Figures 22b and 22e are taken 7.5 min after the encounter when the shear layer is at $X = -7$ R_E, and snapshots in Figures 22c and 22f are taken 19.5 min after encounter when the shear layer is at $X = -41$ R_E.

magnetotail re-orientation with respect to the ionosphere (cf. Figure 22).

[65] The catastrophic disconnections of the tailward-flowing distant magnetotail seen in the simulations of section 4 probably do not have any effects on the operation of the near-Earth portions of the magnetosphere. In a sense they are events happening to material that is already being exhausted from the magnetospheric system. Note however that simulations of the tail behavior for magnetically closed magnetotails under northward IMF have not yet been performed. Disconnecting a closed-field portion of the magnetotail might have a feed-back effect on the rest of the nightside magnetosphere.

5.3. Comet Analogy

[66] For the Earth's magnetotail, reconnection driven partial disconnections associated with geomagnetic substorms have been considered in the past [e.g., *Hones et al.*, 1984; *Fairfield*, 1986; *Cowley*, 1991]; the disconnections considered here are complete, akin to the disconnection events seen in comet plasma tails (Type-I tails). The magnetotail disconnections studied here have some analogies with comet-tail disconnections and some differences. Studies of comet-tail disconnections present an important lesson for the study of disconnections of the Earth's magnetotail.

[67] For quite some time it has been realized that comet ionic tails are controlled by a plasma flow from the Sun [*Hoffmeister*, 1943; *Biermann*, 1951; *Alfvén*, 1957; *Lust*, 1959, 1962; *Stumpff*, 1961], even before the presence of a solar wind had been confirmed by spacecraft measurements [*Gringauz et al.*, 1960; *Coleman et al.*, 1960]. Comet plasma tails have been utilized to study the basic properties of the solar wind [*Lust*, 1959; *Harwit and Hoyle*, 1962; *Clover et al.*, 2010], including solar-activity related variations in the solar wind [*Lust*, 1961; *Jockers and Lust*, 1973; *Jockers*, 1981; *Miller*, 1976] and heliospheric-latitudinal variations of the solar wind properties [*Stumpff*, 1961; *Brandt and Snow*, 2000; *Snow et al.*, 2004]. Temporal changes in the comet tails have been associated with spatial structures in the convected solar wind [*Lust*, 1962, *Niedner et al.*, 1978; *Miller*, 1979; *Yi et al.*, 1994; *Vourlidas et al.*, 2007; *Kuchar et al.*, 2008]. Of particular interest for the present study, variations of the orientations of comet tails have been used to study the variability of the flow direction of the solar wind [*Brandt*, 1968a; *Brandt and Hardorp*, 1970; *Brandt and Heise*, 1970; *Brandt et al.*, 1972; *Tarashuchuk*, 1976] and kinks, wiggles, and knots in the comet tails have been used to study temporal variations in the solar wind flow vector [*Schlosser and Hardorp*, 1968; *Brandt et al.*, 1980; *Fulle and Pansecchi*, 1984; *Jockers*, 1985; *Buffington et al.*, 2008] with the comet tail passively reacting to the solar wind. Other pictures attribute the kinks, knots, and disconnections of comet plasma tails to flow instabilities (e.g., Kelvin-Helmholtz) between the comet plasma and the solar wind [*Ershkovich et al.*, 1973; *Ershkovich*, 1980; *Gestrin and Kontorovich*, 1984; *Wang*, 1991]. Reviews of the study of the interaction of the solar wind with comet plasma tails can be found in *Biermann and Lust* [1963], *Brandt* [1968b], *Miller* [1976], and *Mendis* [2007].

[68] Simulations of the interaction of the solar wind with comets to produce plasma tails appear in *Ogino et al.* [1988] and *Gombosi et al.* [1996, 1997]; the simulations point out an important difference between the comet plasma tail and the Earth's magnetotail, namely that the tail magnetic field of the comet does not connect to the comet body, only into the plasma produced by gas outflow from the comet body. (Hence, tail disconnections in a comet could be caused by reconnection on the dayside.) MHD simulations of the dynamical reaction of comet plasma tails to changes in the solar wind have been performed numerous times [*Ogino et al.*, 1986; *Schmidt-Voigt*, 1989; *Yi et al.*, 1996; *Jia et al.*, 2009], including the reaction to changes that have included sudden changes in the solar wind flow vector (wind shears) [*Rauer et al.*, 1995; *Wegmann*, 2000]. The various simulation figures of *Wegmann* [2000] show both slow and sharp bends of the comet tails in response to solar wind velocity shears.

5.4. Future Simulations

[69] The global MHD simulations of this report could be considered as preliminary simulations exploring global effects, with simplified velocity shears and with low-Reynolds-number simulations. Subsequent simulations are needed to fully explore and assess the importance of sudden velocity shears on magnetospheric physics. Some suggested improvements are discussed in the following paragraphs.

[70] Increasing the size of the simulation domain would provide a larger reservoir of solar wind around the magnetotail and would provide more room for the magnetotail to swing without encountering the simulation boundary.

[71] Actual solar wind velocity-shear layers have a $\Delta\underline{B}$ perturbation along with the $\Delta\underline{v}$ perturbation, as elaborated upon in section 3. The $\Delta\underline{B}$ and $\Delta\underline{v}$ perturbations are not independent. Exploring the reaction of the magnetosphere to $\Delta\underline{v}$-only layers, to $\Delta\underline{B}$-only layers, and to combined $\Delta\underline{v}$ and $\Delta\underline{B}$ layers must be done to gain a full understanding of how the shear layers affect the magnetosphere. (Note that such $\Delta\underline{v}$ versus $\Delta\underline{B}$ simulations were performed for comets by *Rauer et al.* [1995] and by *Wegmann* [2000].)

[72] Solar wind velocity-shear layers have various orientations. Examining the effects of the north-south tilt angle and of the east-west yaw angle of the layer orientation on the shear-Earth interaction should be done. (Note that *Wegmann* [2000] has performed some tilted-shear-plane simulations of the solar wind interaction with comets.)

[73] The behavior of the magnetosphere as a spatial sequence of shear layers passes should be examined with simulations. In the fast solar wind, shear layers with $\Delta v >$ 40 km/s are less than 100 R_E apart on average. Also, there is a population of events in the solar wind denoted "pulsed Alfven waves" [*Gosling et al.*, 2011] which are paired parallel shear layers with separations of a few R_E; these pairs of shears have the opposite sign of $\Delta\underline{v}$ so that the plasma between the pair of layers looks like a "flow burst." The reaction of the magnetosphere to such an event could be very interesting.

[74] It is important to look at the effects of sudden wind shears on the Earth's magnetotail under northward IMF when the magnetotail is in a closed state [*Birn et al.*, 1992; *Fedder and Lyon*, 1995; *Fairfield et al.*, 1996], perhaps loaded with cool dense plasma sheet [*Fujimoto et al.*, 2000; *Oieroset et al.*, 2005]. In the simulations of section 4, near-Earth nightside reconnection was ongoing in all four simulation codes. With reconnection ongoing there is plenty

of antisunward flow in the magnetotail and the new tail lengthened at about the solar wind speed when it was sheared off (cf. Figures 12 and 19). Under northward IMF the new tail may not be able to lengthen: hence a disconnection may be more dramatic as a portion of the magnetotail is caught in the shear layer and carried away from the Earth-connected magnetotail.

[75] Higher-resolution MHD simulations are desirable to look for some internal-magnetospheric effects of sudden wind shears. One such effect is substorm activation triggered by the passage of the shear. Higher-resolution grids covering the magnetotail are desirable to look for effects such as current-sheet thinning caused by the rapid tail displacement. The effects of north-south bending versus east-west bending are of interest.

[76] Higher-resolution simulations are also desirable to look for ULF ringing in the dipolar and near-tail regions associated with the reaction to wind shear. Higher-resolution simulations would provide a higher-Q for the magnetospheric cavity to prevent damping of the excitations and would provide better radial isolation of ULF modes to prevent phase mixing of the excitations.

[77] Higher-resolution simulations are also desirable to look at the temporal shift in ionospheric currents and to look for Alfven-wave ringing in those currents in the magnetosphere.

[78] Higher-resolution simulations are also desirable to examine the fate of the remnant magnetotail material caught up in the velocity-shear layer. Knowing whether or not this material becomes rolled up and mixed and whether or not the magnetotail magnetic fields are induced to reconnect will help to predict what such an event would look like in measurements from a deep-tail spacecraft.

5.5. Needed Data-Analysis Studies

[79] A number of magnetotail and ionospheric phenomena need to be examined in connection with the passage of velocity-shear layers in the solar wind.

[80] Whether or not there are intensifications of ULF-oscillation levels in the dipolar regions of the magnetosphere temporally associated with the passage of wind shears should be established. This would help our understanding of the stormtime energization of the electron radiation belts and would have implications as to the importance of Alfvenic fluctuations during high-speed-stream-driven storms [cf. *Tsurutani and Gonzalez*, 1987; *Denton et al.*, 2008].

[81] An examination should be made of the shift in high-latitude ionospheric currents associated with the passage of velocity-shear layers and the changes of the windsock angle of the magnetotail. The changing of the currents could be monitored on slow timescales with high-resolution magnetometer arrays [*Waters et al.*, 2001] and at higher time resolution with polar radar networks [*Sofko et al.*, 1995]. A shift in the ionospheric convection pattern should also occur as the shear layer passes the Earth.

[82] A temporal association between wind shears and substorm-onset occurrence should be thoroughly studied. It was noted in section 5.B that a preliminary study of this found no temporal association.

[83] The change in the magnetotail windsock angle with sudden changes in the solar wind flow vector was established by *Hones et al.* [1986] using IMP-8 measurements of the solar wind and ISEE-3 measurements of the magnetotail at $\sim$235 R_E downtail. Correlating the occurrence times of spacecraft magnetopause crossings and neutral-sheet crossings with the passages of velocity shears should be performed.

[84] **Acknowledgments.** The author thanks Joachim Birn, John Lyon, Masha Kuznetsova, Steve Morley, Lutz Rastaetter, Ruth Skoug, John Steinberg, and Dan Welling for help and for helpful conversations. All simulations were performed at the Community Coordinated Modeling Center (CCMC) at NASA/Goddard Space Flight Center. The CCMC is a multiagency partnership between NASA, NSF, AFMC, AFOSR, AFRL, AFWA, NOAA, and ONR. This work was supported by the NASA Heliospheric SR&T program, the NASA Heliospheric Guest-Investigator program, the NASA CCMSM-24 program, and the NSF SHINE program.

[85] Philippa Browning thanks Tiera Laitinen and another reviewer for their assistance in evaluating this paper.

References

Alevizos, A., J. Plygiannakis, A. Kakouris, and X. Moussas (1999), A method for spherical harmonic analysis of Compton-Getting corrected 3-D energetic particle distributions, *Sol. Phys.*, *186*, 401, doi:10.1023/A:1005145021168.

Alfvén, H. (1957), On the theory of comet tails, *Tellus*, *9*, 92, doi:10.1111/j.2153-3490.1957.tb01855.x.

Anderson, B. J., M. J. Engebretson, S. P. Rounds, L. J. Zanetti, and T. A. Potemra (1990), A statistical study of Pc 3–5 pulsations observed by the AMPTE/CCE magnetic fields experiment: 1. Occurrence distributions, *J. Geophys. Res.*, *95*, 10,495, doi:10.1029/JA095iA07p10495.

Bavassano, B., and R. Bruno (1992), On the role of interplanetary sources in the evolution of low-frequency Alfvenic turbulence in the solar wind, *J. Geophys. Res.*, *97*, 19,129, doi:10.1029/92JA01510.

Belcher, J. W., and L. Davis (1971), Large-amplitude Alfven waves in the interplanetary medium, 2, *J. Geophys. Res.*, *76*, 3534, doi:10.1029/JA076i016p03534.

Bellaire, P. J. (2004), Space weather research in the US Air Force Office of Scientific Research, in *Effects of Space Weather on Technology Infrastructure*, edited by I. A. Daglis, p. 319, Kluwer Academic, Dordrecht, Netherlands, doi:10.1007/1-4020-2754-0_17.

Bellaire, P. J. (2006), Community Coordinated Modeling Center 2005 Workshop report, *Space Weather*, *4*, S02004, doi:10.1029/2005SW000206.

Biermann, L. (1951), Kometenschweife und solare Korpuskularstrahlung, *Z. Astrophys.*, *29*, 274.

Biermann, L., and R. Lust (1963), Comets: Structure and dynamics of tails, in *The Moon Meteorites and Comets*, edited by B. M. Middlehurst and G. P. Kuiper, pp. 618–638, Univ. of Chicago Press, Chicago, Ill.

Birn, J., G. Yur, H. U. Rahman, and S. Minaami (1992), On the termination of the closed field line region of the magnetotail, *J. Geophys. Res.*, *97*, 14,833, doi:10.1029/92JA01145.

Biskamp, D., and H. Welter (1989), Dynamics of decaying two-dimensional magnetoghydrodynamic turbulence, *Phys. Fluids B*, *1*, 1964.

Borovsky, J. E. (2006), The eddy viscosity and flow properties of the solar wind: CIRs, CME sheaths, and solar-wind/magnetosphere coupling, *Phys. Plasmas*, *13*, 056505, doi:10.1063/1.2200308.

Borovsky, J. E. (2008), The flux-tube texture of the solar wind: Strands of the magnetic carpet at 1 AU?, *J. Geophys. Res.*, *113*, A08110, doi:10.1029/2007JA012684.

Borovsky, J. E. (2010), On the variations of the solar-wind magnetic field about the Parker-spiral direction, *J. Geophys. Res.*, *115*, A09101, doi:10.1029/2009JA015040.

Borovsky, J. E. (2012a), The velocity and magnetic-field fluctuations of the solar wind at 1 AU: Statistical analysis of Fourier spectra and correlations with plasma properties, *J. Geophys. Res.*, *117*, A05104, doi:10.1029/2011JA017499.

Borovsky, J. E. (2012b), Looking for evidence of mixing in the solar wind from 0,31 to 0.98 AU, *J. Geophys. Res.*, doi:10.1029/2012JA017525, in press.

Borovsky, J. E., and M. H. Denton (2010a), Solar-wind turbulence and shear: A superposed-epoch analysis of corotating interaction regions at 1 AU, *J. Geophys. Res.*, *115*, A10101, doi:10.1029/2009JA014966.

Borovsky, J. E., and M. H. Denton (2010b), The magnetic field at geosynchronous orbit during high-speed-stream-driven storms: Connections to the solar wind, the plasma sheet, and the outer electron radiation belt, *J. Geophys. Res.*, *115*, A08217, doi:10.1029/2009JA015116.

Borovsky, J. E., and M. H. Denton (2011), No evidence for the heating of the solar wind at strong current sheets, *Astrophys. J.*, *739*, L61, doi:10.1088/2041-8205/739/2/L61.

Borovsky, J. E., and S. P. Gary (2009), On viscosity and the Reynolds number of MHD turbulence in collisionless plasmas: Coulomb collisions,

Landau damping, and Bohm diffusion, *Phys. Plasmas*, *16*, 082307, doi:10.1063/1.3155134.
Borovsky, J. E., and S. P. Gary (2011), Electron-ion Coulomb scattering and the electron Landau damping of Alfven waves in the solar wind, *J. Geophys. Res.*, *116*, A07101, doi:10.1029/2010JA016403.
Borovsky, J. E., M. Hesse, J. Birn, and M. M. Kuznetsova (2008), What determines the reconnection rate at the dayside magnetosphere?, *J. Geophys. Res.*, *113*, A07210, doi:10.1029/2007JA012645.
Brandt, J. C. (1968a), Ionic comet tails and peculiar motions in the solar wind, *Astron. J.*, *73*, S6.
Brandt, J. C. (1968b), The physics of comet tails, *Annu. Rev. Astron. Astrophys.*, *6*, 267, doi:10.1146/annurev.aa.06.090168.001411.
Brandt, J. C., and J. Hardorp (1970), Ionic comet tails and the direction of the solar wind, *Astron. Astrophys.*, *5*, 322.
Brandt, J. C., and J. Heise (1970), Interplanetary gas. XV. Nonradial plasma motions from the orientations of comet tails, *Astrophys. J.*, *159*, 1057, doi:10.1086/150383.
Brandt, J. C., and M. Snow (2000), Heliospheric latitude variations of properties of cometary plasma tails: A test of the Ulysses Comet watch paradigm, *Icarus*, *148*, 52, doi:10.1006/icar.2000.6484.
Brandt, J. C., R. G. Roosen, and R. S. Harrington (1972), Interplanetary gas. XVII. An astrometric determination of solar-wind velocities from orientations of ionic comet tails, *Astrophys. J.*, *177*, 277, doi:10.1086/151706.
Brandt, J. C., J. D. Hawley, and M. B. Niedner (1980), A very rapid turning of the plasma-tail of Comet Brandfield 1979l on 1980 February 6, *Astrophys. J.*, *241*, L51, doi:10.1086/183359.
Bruno, R., V. Carbone, P. Veltri, E. Pietropaolo, and B. Bavassano (2001), Identifying intermittency events in the solar wind, *Planet. Space Sci.*, *49*, 1201, doi:10.1016/S0032-0633(01)00061-7.
Buffington, A., M. M. Bisi, J. M. Clover, P. P. Hick, B. V. Jackson, and T. A. Kuchar (2008), Analysis of plasma-tail motions for Comets C/2001 Q4(NEAT) and C/200 T7(LINEAR) using observations from SMEI, *Astrophys. J.*, *677*, 798, doi:10.1086/529039.
Burgess, D. (1989), On the effect of a tangential discontinuity on ions specularly reflected at an oblique shock, *J. Geophys. Res.*, *94*, 472, doi:10.1029/JA094iA01p00472.
Burlaga, L. F. (1968), Micro-scale structures in the interplanetary medium, *Sol. Phys.*, *4*, 67, doi:10.1007/BF00146999.
Burlaga, L. F. (1969), Directional discontinuities in the interplanetary magnetic field, *Sol. Phys.*, *7*, 54, doi:10.1007/BF00148406.
Burlaga, L. F. (1971), Nature and origin of directional discontinuities in the solar wind, *J. Geophys. Res.*, *76*, 4360, doi:10.1029/JA076i019p04360.
Burlaga, L. F., and N. F. Ness (1969), Tangential discontinuities in the solar wind, *Sol. Phys.*, *9*, 467, doi:10.1007/BF02391672.
Burrell, K. H. (1997), Effects of ExB velocity shear and magnetic shear on turbulence and transport in magnetic confinement devices, *Phys. Plasmas*, *4*, 1499, doi:10.1063/1.872367.
Chen, H., and D. Montgomery (1987), Turbulent MHD transport coefficients: An attempt at self-consistency, *Plasma Phys. Controlled Fusion*, *29*, 205, doi:10.1088/0741-3335/29/2/006.
Clover, J. M., B. V. Jackson, A. Buffington, P. Hicks, and M. M. Bisi (2010), Solar wind speed inferred from cometary plasma tails using observations from STEREO HI-1, *Astrophys. J.*, *713*, 394, doi:10.1088/0004-637X/713/1/394.
Coleman, P. J. (1968), Turbulence, viscosity, and dissipation in the solar-wind plasma, *Astrophys. J.*, *153*, 371, doi:10.1086/149674.
Coleman, P. J., L. Davis, and C. P. Sonett (1960), Steady component of the interplanetary magnetic field: Pioneer V, *Phys. Rev. Lett.*, *5*, 43, doi:10.1103/PhysRevLett.5.43.
Cowley, S. W. H. (1991), The structure and length of tail-associated phenomena in the solar wind downstream from the Earth, *Planet. Space Sci.*, *39*, 1039, doi:10.1016/0032-0633(91)90110-V.
Crooker, N. U., G. L. Siscoe, S. Shodhan, D. F. Webb, J. T. Gosling, and E. J. Smith (1993), Multiple heliospheric current sheets and coronal streamer belt dynamics, *J. Geophys. Res.*, *98*, 9371, doi:10.1029/93JA00636.
Crooker, N. U., M. E. Burton, J. L. Phillips, E. J. Smith, and A. Balogh (1996), Heliospheric plasma sheets as small-scale transients, *J. Geophys. Res.*, *101*, 2467, doi:10.1029/95JA03148.
DeForest, C. E., S. P. Plunkett, and M. D. Andrews (2001), Observation of polar plumes at high solar altitudes, *Astrophys. J.*, *546*, 569, doi:10.1086/318221.
Denskat, K. U., and F. M. Neubauer (1982), Properties of low-frequency magnetic field fluctuations in the solar wind from 0.29 to 1.0 AU during solar minimum conditions: HELIOS 1 ad HELIOS 2, *J. Geophys. Res.*, *87*, 2215, doi:10.1029/JA087iA04p02215.
Denton, M. H., J. E. Borovsky, R. B. Horne, R. L. McPherron, S. K. Morley, and B. T. Tsurutani (2008), High-speed solar wind streams: A call for key research, *Eos Trans. AGU*, *89*, 62, doi:10.1029/2008EO070002.
De Zeeuw, D. L., T. I. Gombosi, C. P. T. Groth, K. G. Powell, and Q. F. Stout (2000), An adaptive MHD method for global space weather simulations, *IEEE Trans. Plasma Sci.*, *28*, 1956.
Diamond, P. H., S.-I. Itoh, K. Itoh, and T. S. Hahm (2005), Zonal flows in plasma: A review, *Plasma Phys. Controlled Fusion*, *47*, R35, doi:10.1088/0741-3335/47/5/R01.
Dmitruk, P., D. O. Gomez, and E. E. DeLuca (1998), Magnetohydrodynamic turbulence of coronal active regions and the distribution of nanoflares, *Astrophys. J.*, *505*, 974, doi:10.1086/306182.
Drell, S. D., H. M. Foley, and M. A. Ruderman (1965), Drag and propulsion of large satellite in the ionosphere: An Alfven propulsion engine in space, *J. Geophys. Res.*, *70*, 3131, doi:10.1029/JZ070i013p03131.
Eastwood, J. P., S. J. Schwartz, T. S. Horbury, C. M. Carr, K.-H. Glassmeier, I. Richter, C. Koenders, F. Plaschke, and J. A. Wild (2011), Transient Pc3 wave activity generated by a hot flow anomaly: Cluster, Rosetta, and ground-based observations, *J. Geophys. Res.*, *116*, A08224, doi:10.1029/2011JA016467.
Elkington, S. R., M. K. Hudson, and A. A. Chan (1999), Acceleration of relativistic electrons via drift-resonant interaction with toroidal-mode PC-5 ULF oscillations, *Geophys. Res. Lett.*, *26*, 3273, doi:10.1029/1999GL003659.
Ershkovich, A. I. (1980), Kelvin-Helmholtz instability in type-I comet tails and associated phenomena, *Space Sci. Rev.*, *25*, 3, doi:10.1007/BF00200796.
Ershkovich, A. I., A. A. Nusinov, and A. A. Chernikov (1973), Kelvin-Helmholtz instability in Type I comet tails, *Sov. Astron.*, *16*, 705.
Facskó, G., K. Kecskemety, G. Erdos, M. Tatrallyay, P. W. Daly, and I. Dandouras (2008), A statistical study of hot flow anomalies using Cluster data, *Adv. Space Res.*, *41*, 1286, doi:10.1016/j.asr.2008.02.005.
Fairfield, D. H. (1986), Time variations of the distant magnetotail, *Geophys. Res. Lett.*, *13*, 80, doi:10.1029/GL013i001p00080.
Fairfield, D. H. (1993), Solar wind control of the distant magnetotail: ISEE 3, *J. Geophys. Res.*, *98*, 21,265, doi:10.1029/93JA01847.
Fairfield, D. H., R. P. Lepping, L. A. Frank, K. L. Ackerson, W. R. Patterson, S. Kokubun, T. Yamamoto, K. Tsuruda, and M. Nakamura (1996), Geotail observations of an unusual magnetotail under very northward IMF conditions, *J. Geomagn. Geoelectr.*, *48*, 473, doi:10.5636/jgg.48.473.
Fedder, J. A., and J. G. Lyon (1995), The Earth's magnetosphere is 165 RE long: Self-consistent currents, convection, magnetospheric structure, and processes for northward interplanetary magnetic field, *J. Geophys. Res.*, *100*, 3623, doi:10.1029/94JA02633.
Fejer, J. A., and K. F. Lee (1967), Guided propagation of Alfven waves in the magnetosphere, *J. Plasma Phys.*, *1*, 387, doi:10.1017/S0022377800003408.
Feldman, W. C., J. T. Gosling, D. J. McComas, and J. L. Phillips (1993), Evidence for ion jets in the high-speed solar wind, *J. Geophys. Res.*, *98*, 5593, doi:10.1029/92JA02260.
Fillingim, M. O., J. P. Eastwood, G. K. Parks, V. Angelopoulos, I. R. Mann, S. B. Mende, and A. T. Weatherwax (2011), Polar UVI and THEMIS GMAG observations of the ionospheric response to a hot flow anomaly, *J. Atmos. Sol. Terr. Phys.*, *73*, 137, doi:10.1016/j.jastp.2010.03.001.
Fisk, L. A., and T. H. Zurbuchen (2006), Distribution and properties of open magnetic flux outside of coronal holes, *J. Geophys. Res.*, *111*, A09115, doi:10.1029/2005JA011575.
Freeman, J. W., and R. E. Lopez (1985), The cold solar wind, *J. Geophys. Res.*, *90*, 9885, doi:10.1029/JA090iA10p09885.
Freeman, M. P., and S. K. Morley (2009), No evidence for externally triggered substorms based on superposed epoch analysis of IMF Bz, *Geophys. Res. Lett.*, *36*, L21101, doi:10.1029/2009GL040621.
Fujimoto, M., T. Mukai, A. Matsuoka, Y. Saito, H. Hayakawa, S. Kokubun, and R. P. Lepping (2000), Multi-point observations of cold-dense plasma sheet and its relation with tail-LLBL, *Adv. Space Res.*, *25*, 1607, doi:10.1016/S0273-1177(99)00674-2.
Fulle, M., and L. Pansecchi (1984), A possible solar-wind cause of the segmented appearance and of the changes in orientation of the plasma-tail axis of Comet Austin 1982g, *Icarus*, *57*, 410, doi:10.1016/0019-1035(84)90126-X.
Gabriel, A. H., F. Bely Dubau, and P. Lamaire (2003), The contribution of polar plumes to the fast solar wind, *Astrophys. J.*, *589*, 623, doi:10.1086/374416.
Gestrin, S. G., and V. M. Kontorovich (1984), Wind instability and the helical comet-tail structures, *Sov. Astron. Lett.*, *10*, 329.
Ghosh, S., W. H. Matthaeus, D. A. Roberts, and M. L. Goldstein (1998), The evolution of slab fluctuations in the presence of pressure-balanced

magnetic structures and velocity shears, *J. Geophys. Res.*, *103*, 23,691, doi:10.1029/98JA02195.
Goertz, C. K., and R. W. Boswell (1979), Magnetosphere-ionosphere coupling, *J. Geophys. Res.*, *84*, 7239, doi:10.1029/JA084iA12p07239.
Goldstein, M. L. (2009), Observations and modeling of turbulence in the solar wind, in *Turbulence, Dynamos, Accretion Disks, Pulsars and Collective Plasma Processes: Astrophysics and Space Science Proceedings*, p. 21, Springer, New York,
Goldstein, M. L., D. A. Roberts, A. E. Deane, S. Ghosh, and H. K. Wong (1999), Numerical simulation of Alfvenic turbulence in the solar wind, *J. Geophys. Res.*, *104*, 14,437, doi:10.1029/1998JA900128.
Gombosi, T. I., D. L. De Zeeuw, R. M. Haberli, and K. G. Powell (1996), Three-dimensional multiscale MHD model of cometary plasma environments, *J. Geophys. Res.*, *101*, 15,233, doi:10.1029/96JA01075.
Gombosi, T. I., K. C. Hansen, D. L. De Zeeuw, M. R. Combi, and K. G. Powell (1997), MHD simulation of comets: The plasma environment of Comet Hale-Bopp, *Earth Moon Planets*, *79*, 179, doi:10.1023/A:1006289418660.
Gombosi, T. I., D. L. De Zeeuw, C. P. T. Groth, and K. G. Powell (2000), Magnetospheric configuration for Parker-spiral IMF conditions: Results of a 3D AMR MHD simulation, *Adv. Space Res.*, *26*, 139, doi:10.1016/S0273-1177(99)01040-6.
Gonzalez, W. D., F. L. Guarnieri, A. L. Clua-Gonzalez, E. Echer, M. V. Alves, T. Ogino, and B. T. Tsurutani (2006), Magnetospheric energetics during HILDCAAs, in *Recurrent Magnetic Storms: Corotating Solar Wind Streams*, *Geophys. Monogr. Ser.*, vol. 167, edited by B. Tsurutani et al., p. 175, AGU, Washington, D. C.
Gosling, J. T., H. Tian, and T. D. Phan (2011), Pulsed Alfven waves in the solar wind, *Astrophys. J.*, *737*, L35, doi:10.1088/2041-8205/737/2/L35.
Grappin, R., and M. Velli (1996), Waves and streams in the expanding solar wind, *J. Geophys. Res.*, *101*, 425, doi:10.1029/95JA02147.
Greco, A., W. H. Matthaeus, S. Servidio, P. Chuychai, and P. Dmitruk (2009), Statistical analysis of discontinuities in solar wind ACE data and comparison with intermittent MHD turbulence, *Astrophys. J.*, *691*, L111, doi:10.1088/0004-637X/691/2/L111.
Greenstadt, E. W., D. P. Traver, F. V. Coroniti, E. J. Smith, and J. A. Slavin (1990), Observations of the flank of Earth's bow shock to -100 R_E by ISEE 3/ICE, *Geophys. Res. Lett.*, *17*, 753, doi:10.1029/GL017i006p00753.
Gringauz, K. I., V. V. Bezrukikh, V. D. Ozerov, and R. E. Rybchinskii (1960), A study of the interplanetary ionized gas, high-energy electrons, and corpuscular radiation from the Sun by means of the three-electrode trap for charged particles on the second Soviet cosmic rocket, *Sov. Phys. Dokl.*, Engl. Transl., *5*, 361.
Harwit, M., and F. Hoyle (1962), Plasma dynamics in comets. II. Influence of magnetic fields, *Astrophys. J.*, *135*, 875, doi:10.1086/147331.
Hoffmeister, C. (1943), Physicalische Untersuchunen and Kometen. I. Die Beziehungen des drimaren Schwifstrahls zum Radiusvector, *Z. Asrophys.*, *22*, 263.
Hollweg, J. V., G. Yang, V. M. Cadez, and B. Gakovic (1990), Surface waves in an incompressible fluid: Resonant instability due to velocity shear, *Astrophys. J.*, *349*, 335, doi:10.1086/168317.
Hones, E. W., J. Birn, D. N. Baker, S. J. Bame, J. A. Slavin, E. J. Smith, and B. T. Tsurutani (1984), Detailed examination of a plasmoid in the distant magnetotail with ISEE 3, *Geophys. Res. Lett.*, *11*, 1046, doi:10.1029/GL011i010p01046.
Hones, E. W., R. D. Zwickl, T. A. Fritz, and S. J. Bame (1986), Structural and dynamical aspects of the distant magnetotail determined from ISEE-3 plasma measurements, *Planet. Space Sci.*, *34*, 889, doi:10.1016/0032-0633(86)90001-2.
Horbury, T. S., D. Burgess, M. Franz, and C. J. Owen (2001), Three spacecraft observations of solar wind discontinuities, *Geophys. Res. Lett.*, *28*, 677, doi:10.1029/2000GL000121.
Hsu, T.-S., and R. L. McPherron (2006), The statistical characteristics of IMF triggered substorms, in *Proceedings of the 8th International Conference on Substorms*, edited by M. Syrjasuo and E. Donovan, p. 105, Inst. for Space Res., Calgary, Alberta, Canada.
Ishizawa, A., and Y. Hattori (1998), Large coherent structure formation by magnetic stretching term in two-dimensional MHD turbulence, *J. Phys. Soc. Jpn.*, *67*, 4302, doi:10.1143/JPSJ.67.4302.
Itoh, K., S.-I. Itoh, P. H. Diamond, T. S. Hahm, A. Fujisawa, G. R. Tynan, M. Yagi, and Y. Nagashima (2006), Physics of zonal flows, *Phys. Plasmas*, *13*, 055502, doi:10.1063/1.2178779.
Janhunen, P., M. Palmroth, T. Laitinen, I. Honkonen, L. Juusola, G. Facsko, and T. I. Pulkkinen (2012), The GUMICS-4 global MHD magnetosphere-ionosphere coupling simulation, *J. Atmos. Sol. Terr. Phys.*, *80*, 48, doi:10.1016/j.jastp.2012.03.006.
Jia, Y. D., C. T. Russell, L. K. Jian, W. B. Manchester, O. Cohen, A. Vourlidas, K. C. Hansen, M. R. Combi, and T. I. Gombosi (2009), Study of the 2007 April 20 CME-comet interaction event with an MHD model, *Astrophys. J.*, *696*, L56, doi:10.1088/0004-637X/696/1/L56.
Jockers, K. (1981), Plasma dynamics in the tail of Comet Kohoutek 1973 XII, *Icarus*, *47*, 397, doi:10.1016/0019-1035(81)90188-3.
Jockers, K. (1985), The ion tail of Comet Kohoutek 1973 XII during 17 days of solar wind gusts, *Astron. Astrophys. Suppl. Ser.*, *62*, 791.
Jockers, K., and R. Lust (1973), Tail peculiarities in Comet Bennett caused by solar wind disturbances, *Astron. Astrophys.*, *26*, 113.
Kaghashvili, E. K. (1999), Linear mechanism of Alfven wave dissipation induced by velocity shear: Phase mixing and damping, *AIP Conf. Proc.*, *471*, 345, doi:10.1063/1.58768.
Kivelson, M. G., and W. J. Hughes (1990), On the threshold for triggering substorms, *Planet. Space Sci.*, *38*, 211, doi:10.1016/0032-0633(90)90085-5.
Klein, L., D. A. Roberts, and M. L. Goldstein (1991), Anisotropy and minimum variance directions of solar wind fluctuations in the outer heliosphere, *J. Geophys. Res.*, *96*, 3779, doi:10.1029/90JA02240.
Klein, L., R. Bruno, B. Bavassano, and H. Rosenbauer (1993), Anisotropy and minimum variance of magnetohydrodynamic fluctuations in the inner heliosphere, *J. Geophys. Res.*, *98*, 17,461, doi:10.1029/93JA01522.
Knetter, T., F. M. Neubauer, T. Horbury, and A. Balogh (2003), Discontinuity observations with Cluster, *Adv. Space Res.*, *32*(4), 543, doi:10.1016/S0273-1177(03)00335-1.
Knetter, T., F. M. Neubauer, T. Horbury, and A. Balogh (2004), Four-point discontinuity observations using Cluster magnetic field data: A statistical survey, *J. Geophys. Res.*, *109*, A06102, doi:10.1029/2003JA010099.
Korzhov, N. P., V. V. Mishin, and V. M. Tomozov (1984), On the role of plasma parameters and the Kelvin-Helmholtz instability in a viscous interaction of solar wind streams, *Planet. Space Sci.*, *32*, 1169, doi:10.1016/0032-0633(84)90142-9.
Korzhov, N. P., V. V. Mishin, and V. M. Tomozov (1985), On the viscous interaction of solar wind streams, *Sov. Astron.*, Engl. Transl., *29*, 215.
Koval, A., J. Safrankova, and Z. Nemecek (2005), A study of particle flows in hot flow anomalies, *Planet. Space Sci.*, *53*, 41, doi:10.1016/j.pss.2004.09.027.
Kuchar, T. A., A. Buffington, C. N. Arge, P. P. Hick, T. A. Howard, B. V. Jackson, J. C. Johnson, D. R. Mizuno, S. J. Tappan, and D. F. Webb (2008), Observations of a comet tail disruption induced by the passage of a CME, *J. Geophys. Res.*, *113*, A04101, doi:10.1029/2007JA012603.
Lazarian, A., and E. T. Vishniac (1999), Reconnection in a weakly stochastic field, *Astrophys. J.*, *517*, 700, doi:10.1086/307233.
Lee, L. C., and J. V. Olson (1980), Kelvin-Helmholtz instability and the variation of geomagnetic pulsation activity, *Geophys. Res. Lett.*, *7*, 777, doi:10.1029/GL007i010p00777.
Liemohn, M. W., R. Ilie, N. Y. Ganushkina, A. J. Ridley, J. U. Kozyra, M. F. Thomsen, and J. E. Borovsky (2011), Testing the necessity of transient spikes in the storm time ring current drivers, *J. Geophys. Res.*, *116*, A04226, doi:10.1029/2010JA015914.
Liu, W., T. E. Sarris, X. Li, R. Ergun, V. Angelopoulos, J. Bonnell, and K. H. Glassmeier (2010), Solar wind influence on Pc4 and Pc5 ULF wave activity in the inner magnetosphere, *J. Geophys. Res.*, *115*, A12201, doi:10.1029/2010JA015299.
Longcope, D. W., and H. R. Strauss (1993), The coalescence instability and the development of current sheets in two-dimensional magnetohydrodynamics, *Phys. Fluids B*, *5*, 2858, doi:10.1063/1.860673.
Lust, R. (1959), Die Bewegung von Schwefmaterie des Kometen Mrkos (1957d), *Z. Astrophys.*, *47*, 205.
Lust, R. (1961), Aktivitat von Kometenschweifen in Perioden geomagnetisher Ruhe, *Z. Astrophys.*, *51*, 163.
Lust, R. (1962), Die Bewegung und Form von Sturkturen im Schweif des Kometen Mykow 1957d, *Z. Astrophys.*, *54*, 67.
Lyon, J. G., J. A. Fedder, and C. M. Mobarry (2004), The Lyon-Fedder-Mobarry (LFM) global MHD magnetospheric simulation code, *J. Atmos. Sol. Terr. Phys.*, *66*, 1333, doi:10.1016/j.jastp.2004.03.020.
Lyons, L. R., G. T. Blanchard, J. C. Samson, R. P. Lepping, T. Yamamoto, and T. Moretto (1996), Coordinated observations demonstrating external substorm triggering, *J. Geophys. Res.*, *101*, 13,011, doi:10.1029/95JA01987.
Lyons, L. R., D.-Y. Lee, H.-J. Kim, J. A. Hwang, R. M. Thorne, R. B. Horne, and A. J. Smith (2009), Solar-wind-magnetosphere coupling, including relativistic electron energization, during high-speed streams, *J. Atmos. Sol. Terr. Phys.*, *71*, 1059, doi:10.1016/j.jastp.2008.04.016.
Maezawa, K., T. Hori, T. Mukai, Y. Saito, T. Yamamoto, S. Kokubun, and A. Nishida (1997), Structure of the distant magnetotail and its dependence on the IMF By component: Geotail observations, *Adv. Space Sci.*, *20*, 949, doi:10.1016/S0273-1177(97)00503-6.
Malara, F. (1999), Theoretical aspects of MHD turbulence in the presence of large scale structures, *AIP Conf. Proc.*, *471*, 155, doi:10.1063/1.58744.

Malara, F., L. Primavera, and P. Veltri (1996), Compressive fluctuations generated by time evolution of Alfvenic perturbations in the solar wind current sheet, *J. Geophys. Res.*, *101*, 21,597, doi:10.1029/96JA01637.

Markovskii, S. A., B. J. Vasquez, C. W. Smith, and J. V. Hollweg (2006), Dissipation of the perpendicular turbulent cascade in the solar wind, *Astrophys. J.*, *639*, 1177, doi:10.1086/499398.

Maron, J., and P. Goldreich (2001), Simulations of incompressible magneto-hydrodynamic turbulence, *Astrophys. J.*, *554*, 1175, doi:10.1086/321413.

Marsch, E., K. H. Muhlhauser, R. Schwenn, H. Rosenbauer, W. Pilip, and F. M. Neubauer (1982), Solar wind protons: Three-dimensional velocity distributions and derived plasma parameters measured between 0.3 and 1 AU, *J. Geophys. Res.*, *87*, 52, doi:10.1029/JA087iA01p00052.

Mathie, R. A., and I. R. Mann (2000), A correlation between extended intervals of ULF wave power and storm-time geosynchronous relativistic electron flux enhancements, *Geophys. Res. Lett.*, *27*, 3261, doi:10.1029/2000GL003822.

McComas, D. J., S. J. Blame, P. Barker, W. C. Feldman, J. L. Phillips, P. Riley, and J. W. Griffee (1998), Solar Wind Electron Proton Alpha Monitor (SWEPAM) for the Advanced Composition Explorer, *Space Sci. Rev.*, *86*, 563, doi:10.1023/A:1005040232597.

McPherron, R. L., D. N. Baker, and N. U. Crooker (2009), Role of the Russell-McPherron effect in the acceleration of relativistic electrons, *J. Atmos. Sol. Terr. Phys.*, *71*, 1032, doi:10.1016/j.jastp.2008.11.002.

Mendis, D. A. (2007), The solar-comet interactions, in *Handbook of the Solar-Terrestrial Environment*, edited by Y. Kamide and A. Chain, pp. 493–515, Springer, Berlin.

Menk, F. W., T. K. Yeoman, D. M. Wright, M. Lester, and F. Honary (2003), High-latitude observations of impulse-driven ULF pulsations in the ionosphere ad on the ground, *Ann. Geophys.*, *21*, 559, doi:10.5194/angeo-21-559-2003.

Merka, J., and A. Szabo (2004), Bow shock's geometry at the magnetospheric flanks, *J. Geophys. Res.*, *109*, A12224, doi:10.1029/2004JA010567.

Migliuolo, S. (1984), Velocity shear instabilities in the anisotropic solar wind and the heating of ions perpendicular to the magnetic field, *J. Geophys. Res.*, *89*, 27, doi:10.1029/JA089iA01p00027.

Miller, F. D. (1976), Solar-cometary relations and the events of June-August 1972, *Space Sci. Rev.*, *19*, 739, doi:10.1007/BF00210649.

Miller, F. D. (1979), Comet Tago-Sato-Kosaka 1969 IX: Tail structure 25 December 1969 to 12 January 1970, *Icarus*, *37*, 443, doi:10.1016/0019-1035(79)90007-1.

Miller, R. S., F. Mashayek, V. Adumitroaie, and P. Givi (1996), Structure of homogeneous nonhelical magnetohydrodynamic turbulence, *Phys. Plasmas*, *3*, 3304, doi:10.1063/1.871599.

Mininni, P., A. G. Pouquet, and D. C. Montgomery (2006), Small-scale structures in three-dimensional magnetohydrodynamic turbulence, *Phys. Rev. Lett.*, *97*, 244503, doi:10.1103/PhysRevLett.97.244503.

Morley, S. K., and M. P. Freeman (2007), On the association between northward turnings of the interplanetary magnetic field and substorm onsets, *Geophys. Res. Lett.*, *34*, L08104, doi:10.1029/2006GL028891.

Nakagawa, T. (1993), Solar source of the interplanetary planar magnetic structures, *Sol. Phys.*, *147*, 169, doi:10.1007/BF00675493.

Nakagawa, T., A. Nishida, and T. Saito (1989), Planar magnetic structures in the solar wind, *J. Geophys. Res.*, *94*, 11,761, doi:10.1029/JA094iA09p11761.

Naulin, V., A. Kendl, O. E. Garcia, A. H. Nielsen, and J. J. Rasmussen (2005), Shear flow generation and energetics in electromagnetic turbulence, *Phys. Plasmas*, *12*, 052515, doi:10.1063/1.1905603.

Neugebauer, M. (1985), Alignment of velocity and field changes across tangential discontinuities in the solar wind, *J. Geophys. Res.*, *90*, 6627, doi:10.1029/JA090iA07p06627.

Neugebauer, M., D. R. Clay, B. E. Goldstein, B. T. Tsurutani, and R. D. Zwickl (1984), A reexamination of rotational and tangential discontinuities in the solar wind, *J. Geophys. Res.*, *89*, 5395, doi:10.1029/JA089iA07p05395.

Neugebauer, M., C. J. Alexander, R. Schwenn, and A. K. Richter (1986), Tangential discontinuities in the solar wind: Correlated field and velocity changes and the Kelvin-Helmholtz instability, *J. Geophys. Res.*, *91*, 13,694, doi:10.1029/JA091iA12p13694.

Niedner, M. B., E. D. Rothe, and J. C. Brandt (1978), Interplanetary gas. XXII. Interaction of Comet Kohoutek's ion tail with the compression region of a solar-wind corotating stream, *Astrophys. J.*, *221*, 1014, doi:10.1086/156107.

Ogino, T., R. J. Walker, and M. Ashour-Abdalla (1986), A three-dimensional MHD simulation of the interaction of the solar wind with the outflowing plasma from a comet, *Geophys. Res. Lett.*, *13*, 929, doi:10.1029/GL013i009p00929.

Ogino, T., R. J. Walker, and M. Ashour-Abdalla (1988), An MHD simulation of the interaction of the solar wind with Comet Halley, *J. Geophys. Res.*, *93*, 9568, doi:10.1029/JA093iA09p09568.

Oieroset, M., J. Raeder, T. D. Phan, S. Wing, J. P. McPhadden, W. Li, M. Fujimoto, H. Reme, and A. Balogh (2005), Global cooling and densification of the plasma sheet during an extended period of purely northward IMF on October 22–24, 2003, *Geophys. Res. Lett.*, *32*, L12S07, doi:10.1029/2004GL021523.

Owen, C. J., J. A. Slavin, I. G. Richardson, N. Murphy, and R. J. Hynds (1995), Average motion, structure and orientation of the distant magnetotail determined from remote sensing of the edge of the plasma sheet boundary layer with E > 35 keV ions, *J. Geophys. Res.*, *100*, 185, doi:10.1029/94JA02417.

Pariat, E., S. K. Antiochos, and C. R. DeVore (2009), A model for solar polar jets, *Astrophys. J.*, *691*, 61, doi:10.1088/0004-637X/691/1/61.

Parker, E. N. (1969), Theoretical studies of the solar wind phenomenon, *Space Sci. Rev.*, *9*, 325, doi:10.1007/BF00175236.

Parker, E. N. (1994), *Spontaneous Current Sheets in Magnetic Fields*, Oxford Univ. Press, New York.

Parker, E. N. (2004), Tangential discontinuities in untidy magnetic topologies, *Phys. Plasmas*, *11*, 2328, doi:10.1063/1.1646674.

Paterson, W. R., and L. A. Frank (1994), Survey of plasma parameters in Earth's distant magnetotail with the Geotail spacecraft, *Geophys. Res. Lett.*, *21*, 2971, doi:10.1029/94GL02105.

Paulikas, G. A., and J. B. Blake (1979), Effects of the solar wind on magnetospheric dynamics: Energetic electrons at the synchronous orbit, in *Quantitative Modeling of Magnetospheric Processes*, *Geophys. Monogr. Ser.*, vol. 21, edited by W. P. Olson, p. 180, AGU, Washington, D. C., doi:10.1029/GM021p0180.

Phillips, J. L., S. J. Bame, S. P. Gary, J. T. Gosling, E. E. Scime, and R. J. Forsyth (1995), Radial and meridional trends in solar wind thermal electron temperature and anisotropy: Ulysses, *Space Sci. Rev.*, *72*, 109, doi:10.1007/BF00768763.

Pilipenko, V., O. Kozyreva, V. Belakhovsky, M. J. Engebretson, and S. Samsonov (2010), Generation of magnetic and particle Pc5 pulsations during the recovery phase of strong magnetic storms, *Proc. R. Soc. A*, *466*, 3363, doi:10.1098/rspa.2010.0079.

Pilipp, W. G., H. Miggenrieder, K.-H. Muhlhauser, H. Rosenbauer, and R. Schwenn (1990), Large scale variations of thermal electron parameters in the solar wind between 0.3 and 1 AU, *J. Geophys. Res.*, *95*, 6305, doi:10.1029/JA095iA05p06305.

Potapov, A. S., and T. N. Polyushkina (2010), Experimental evidence for direct penetration of ULF waves from the solar wind and their possible effect on acceleration of radiation belt electrons, *Geomagn. Aeron.*, *50*, 950, doi:10.1134/S0016793210080049.

Powell, K., P. Roe, T. Linde, T. Gombosi, and D. L. De Zeeuw (1999), A solution-adaptive upwind scheme for ideal magnetohydrodynamics, *J. Comput. Phys.*, *154*, 284, doi:10.1006/jcph.1999.6299.

Raeder, J. (1999), Modeling the magnetosphere for northward interplanetary magnetic field: Effects of electrical resistivity, *J. Geophys. Res.*, *104*, 17,357, doi:10.1029/1999JA900159.

Raeder, J., Y. L. Wang, T. J. Fuller-Rowell, and H. J. Singer (2001), Global simulation of magnetospheric space weather effects of the Bastille day storm, *Sol. Phys.*, *204*, 323, doi:10.1023/A:1014228230714.

Rauer, H., R. Wegmann, H. U. Schmidt, and K. Jockers (1995), 3-D MHD simulations of the effect of commoving discontinuities in the solar wind on cometary plasma tails, *Astron. Astrophys.*, *295*, 529.

Reeves, G. D., S. K. Morley, R. H. W. Friedel, M. G. Henderson, T. E. Cayton, G. Cunningham, J. B. Blake, R. A. Christensen, and D. Thomsen (2011), On the relationship between relativistic electron flux and solar wind velocity: Paulikas and Blake revisited, *J. Geophys. Res.*, *116*, A02213, doi:10.1029/2010JA015735.

Riazantseva, M. O., G. N. Zastenker, and J. D. Richardson (2005a), The characteristics of sharp (small-scale) boundaries of solar wind plasma and magnetic field structures, *Adv. Space Res.*, *35*, 2147, doi:10.1016/j.asr.2004.12.011.

Riazantseva, M. O., G. N. Zastenker, J. D. Richardson, and P. E. Eiges (2005b), Sharp boundaries of small- and middle-scale solar wind structures, *J. Geophys. Res.*, *110*, A12110, doi:10.1029/2005JA011307.

Richardson, J. D., and K. I. Paularena (2001), Plasma and magnetic field correlations in the solar wind, *J. Geophys. Res.*, *106*, 239, doi:10.1029/2000JA000071.

Richardson, J. D., K. I. Paularena, A. J. Lazarus, and J. W. Belcher (1995), Radial evolution of the solar wind from IMP 8 to Voyager 2, *Geophys. Res. Lett.*, *22*, 325, doi:10.1029/94GL03273.

Roberts, D. A., and S. Ghosh (1999), A kinematic analysis of the role of velocity shear in expanding plasmas, *J. Geophys. Res.*, *104*, 22,395, doi:10.1029/1999JA900272.

Roberts, D. A., L. W. Klein, M. L. Goldstein, and W. H. Matthaeus (1987), Nature and evolution of magnetohydrodynamic fluctuations in the solar wind: Helios observations and Helios-Voyager comparisons, *J. Geophys. Res.*, *92*, 12,023, doi:10.1029/JA092iA11p12023.

Roberts, D. A., M. L. Goldstein, W. H. Matthaeus, and S. Ghosh (1992), Velocity shear generation of solar wind turbulence, *J. Geophys. Res.*, *97*, 17,115, doi:10.1029/92JA01144.

Rosenbauer, H., R. Schwenn, E. Marsch, B. Meyer, H. Miggenrieder, M. D. Montgomery, K. H. Muhlhauser, W. Pilipp, W. Voges, and S. M. Zink (1977), A survey on initial results of the Helios plasma experiment, *J. Geophys. Res.*, *42*, 561.

Rostoker, G. (1983), Triggering of expansive phase intensifications of magnetospheric substorms by northward turnings of the interplanetary magnetic field, *J. Geophys. Res.*, *88*, 6981, doi:10.1029/JA088iA09p06981.

Ruderman, M. S., M. L. Goldstein, D. A. Roberts, A. Deane, and L. Ofman (1999), Alfven wave phase mixing driving by velocity shear in two dimensions, *AIP Conf. Proc.*, *471*, 337, doi:10.1063/1.58808.

Safrankova, J., L. Prech, Z. Nemecek, D. G. Sibeck, and T. Mukai (2000), Magnetosheath response to the interplanetary magnetic field tangential discontinuity, *J. Geophys. Res.*, *105*, 25,113, doi:10.1029/1999JA000435.

Sanny, J., D. Judnick, M. B. Moldwin, D. Berube, and D. G. Sibeck (2007), Global profiles of compressional ultralow frequency wave power at geosynchronous orbit and their response to the solar wind, *J. Geophys. Res.*, *112*, A05224, doi:10.1029/2006JA012046.

Schliecker, G. (2002), Structure and dynamics of cellular systems, *Adv. Phys.*, *51*, 1319, doi:10.1080/00018730210140814.

Schlosser, W., and J. Hardorp (1968), Die Welligkeit der Schweifstrahlen des Kometen Morehouse 1908 III, *Z. Astrophys.*, *69*, 228.

Schmidt-Voigt, M. (1989), Time-dependent MHD simulations for cometary plasmas, *Astron. Astrophys.*, *210*, 433.

Schwartz, S. J., and E. Marsch (1983), Radial evolution of a single solar wind plasma parcel, *J. Geophys. Res.*, *88*, 9919, doi:10.1029/JA088iA12p09919.

Schwartz, S. J., G. Paschmann, N. Sckopke, T. M. Bauer, M. Dunlop, A. N. Fazakeley, and M. F. Thomsen (2000), Conditions for the formation of hot flow anomalies at Earth's bow shock, *J. Geophys. Res.*, *105*, 12,639, doi:10.1029/1999JA000320.

Shprits, Y. Y., S. R. Elkington, N. P. Meredith, and D. A. Subbotin (2008), Review of modeling of losses and sources of relativistic electrons in the outer radiation belt I: Radial transport, *J. Atmos. Sol. Terr. Phys.*, *70*, 1679, doi:10.1016/j.jastp.2008.06.008.

Sibeck, D. G., G. L. Siscoe, J. A. Slavin, E. J. Smith, B. T. Tsurutani, and R. P. Lepping (1985), The distant magnetotail's response to a strong interplanetary magnetic field By: Twisting, flattening, and field line bending, *J. Geophys. Res.*, *90*, 4011, doi:10.1029/JA090iA05p04011.

Sibeck, D. G., et al. (1999), Comprehensive study of the magnetospheric response to a hot flow anomaly, *J. Geophys. Res.*, *104*, 4577, doi:10.1029/1998JA900021.

Sibeck, D. G., et al. (2000), Magnetopause motion driven by interplanetary magnetic field, *J. Geophys. Res.*, *105*, 25,155, doi:10.1029/2000JA900109.

Siscoe, G. L., L. Davis, P. J. Coleman, E. J. Smith, and D. E. Jones (1968), Power spectra and discontinuities of the interplanetary magnetic field: Mariner 4, *J. Geophys. Res.*, *73*, 61, doi:10.1029/JA073i001p00061.

Slavin, J. A., E. J. Smith, D. J. Sibeck, D. N. Baker, R. D. Zwickl, and S.-I. Akasofu (1985), An ISEE 3 study of average and substorm conditions in the distant magnetosphere, *J. Geophys. Res.*, *90*, 10,875, doi:10.1029/JA090iA11p10875.

Snow, M., J. C. Brandt, Y. Yi, C. C. Petersen, and H. Mikuz (2004), Comet Hyakutake (C/1996 B2), Spectacular disconnection event and the latitudinal structure of the solar wind, *Planet. Space Sci.*, *52*, 313, doi:10.1016/j.pss.2003.10.001.

Sofko, G. J., R. Greenwald, and W. A. Bristow (1995), Direct determination of large scale magnetospheric field aligned currents with SuperDARN, *Geophys. Res. Lett.*, *22*, 2041, doi:10.1029/95GL01317.

Spreiter, J. R., A. L. Summers, and A. Y. Alksne (1966), Hydromagnetic flow around the magnetosphere, *Planet. Space Sci.*, *14*, 223, doi:10.1016/0032-0633(66)90124-3.

Steinberg, J.-L., and C. Lacombe (1992), An empirical model of the plasma density distribution in the distant Earth magnetosphere, *Geophys. Res. Lett.*, *19*, 2285, doi:10.1029/92GL02490.

Stumpff, P. (1961), Zur Korrelation zwischen dem Auftreten von Kometenschweifen des Typ I und der solaren Korpuskularstrahlung, *Astron. Nachr.*, *286*, 87, doi:10.1002/asna.19612860208.

Takahashi, K., and A. Y. Ukhorskiy (2008), Timing analysis of the relationship between solar wind parameters and geosynchronous Pc5 amplitude, *J. Geophys. Res.*, *113*, A12204, doi:10.1029/2008JA013327.

Tarashuchuk, V. P. (1976), Physical characteristics of the solar wind from data of comet observations, *Rep. TT F-1671*, NASA, Washington, D. C.

Terry, P. W. (2000), Does flow shear suppress turbulence in nonionized flows?, *Phys. Plasmas*, *7*, 1653, doi:10.1063/1.873985.

Thomas, V. A., D. Winske, M. F. Thomsen, and T. G. Onsager (1991), Hybrid simulation of the formation of a hot flow anomaly, *J. Geophys. Res.*, *96*, 11,625, doi:10.1029/91JA01092.

Thomsen, M. F., J. T. Gosling, S. A. Fuselier, and S. J. Bame (1986), Hot, diamagnetic cavities upstream from the Earth's bow shock, *J. Geophys. Res.*, *91*, 2961, doi:10.1029/JA091iA03p02961.

Tripathi, L., A. K. Tiwari, and S. P. Agarwal (2007), Study of cosmic-ray intensity variations associated with anomalous, long-duration high-speed solar wind streams in 2003, *Sol. Phys.*, *241*, 171, doi:10.1007/s11207-006-0256-5.

Tsurutani, B. T., and W. D. Gonzalez (1987), The cause of high-intensity long-duration continuous AE Activity (HILDCAAS): Interplanetary Alfven wave trains, *Planet. Space Sci.*, *35*, 405, doi:10.1016/0032-0633(87)90097-3.

Tsurutani, B. T., and C. M. Ho (1999), A review of discontinuities and Alfven waves in interplanetary space: ULYSSES results, *Rev. Geophys.*, *37*, 517, doi:10.1029/1999RG900010.

Tsurutani, B. T., A. J. Mannucci, B. A. Iijima, A. Komjathy, A. Saiton, T. Tsuda, O. P. Verkhoglyadova, W. D. Gonzalez, and F. L. Guarnieri (2006), Dayside ionospheric (GPS) response to corotating solar wind streams, in *Recurrent Magnetic Storms: Corotating Solar Wind Streams*, *Geophys. Monogr. Ser.*, vol. 167, edited by B. Tsurutani et al., p. 245, AGU, Washington, D. C.

Turner, J. M., and G. L. Siscoe (1971), Orientations of 'rotational' and 'tangential' discontinuities in the solar wind, *J. Geophys. Res.*, *76*, 1816, doi:10.1029/JA076i007p01816.

Vasquez, B. J., and J. V. Hollweg (1999), Formation of pressure-balanced structures and fast waves from nonlinear Alfven waves, *J. Geophys. Res.*, *104*, 4681–4696.

Vasquez, B. J., V. I. Abramenko, D. K. Haggerty, and C. W. Smith (2007), Numerous small magnetic field discontinuities of Bartels rotation 2286 and the potential role of Alfvenic turbulence, *J. Geophys. Res.*, *112*, A11102, doi:10.1029/2007JA012504.

Verma, M. K. (1996), Nonclassical viscosity and resistivity of the solar wind plasma, *J. Geophys. Res.*, *101*, 27,543, doi:10.1029/96JA02324.

Viall, N. M., and L. Kepko, and H. E. Spence (2009), Relative occurrence rates and connection of discrete frequency oscillations in the solar wind density and dayside magnetosphere, *J. Geophys. Res.*, *114*, A01201, doi:10.1029/2008JA013334.

Vourlidas, A., C. J. Davis, C. J. Eyles, S. R. Crothers, R. A. Harrison, R. A. Howard, J. D. Moses, and D. G. Socker (2007), First direct observation of the interaction between a comet and a coronal mass ejection leading to a complete plasma tail disconnection, *Astrophys. J.*, *668*, L79, doi:10.1086/522587.

Wang, S. (1991), A mechanism for the formation of knots, kinks, and disconnection events in the plasma tail of comets, *Astron. Astrophys.*, *243*, 521.

Wang, Y.-M., N. R. Sheeley, D. G. Socker, R. A. Howard, G. E. Brueckner, D. J. Michels, D. Moses, O. C. St. Cyr, A. Llebaria, and J.-P. Delaboudiniere (1998), Observations of correlated white-light and extreme-ultraviolet jets from polar coronal holes, *Astrophys. J.*, *508*, 899, doi:10.1086/306450.

Waters, C. L., and B. J. Anderson, and K. Liou (2001), Estimation of global field aligned currents using Iridium magnetometer data, *Geophys. Res. Lett.*, *28*, 2165, doi:10.1029/2000GL012725.

Wegmann, R. (2000), The effect of some solar-wind disturbances on the plasma tail of a comet: Models and observations, *Astron. Astrophys.*, *358*, 759.

Weimer, D. R., and J. H. King (2008), Improved calculations of interplanetary magnetic field phase front angles and propagation time delays, *J. Geophys. Res.*, *113*, A01105, doi:10.1029/2007JA012452.

Wiltberger, M., R. E. Lopez, and J. G. Lyon (2005), Results from magnetospheric Gedanken experiments using the LFM, *Adv. Space Res.*, *36*, 1797, doi:10.1016/j.asr.2004.11.043.

Yamauchi, Y., S. T. Suess, and T. Sakurai (2003), Relation between polar plumes and fine structure in the solar wind from Ulysses high-latitude observations, *AIP Conf. Proc.*, *679*, 255, doi:10.1063/1.1618589.

Yang, G., and J. V. Hollweg (1991), The effects of velocity shear on the resonance absorption of MHD surface waves: Cold plasma, *J. Geophys. Res.*, *96*, 13,807, doi:10.1029/91JA01407.

Yi, Y., F. M. Caputo, and J. C. Brandt (1994), Disconnection events (DEs) and sector boundaries: The evidence from comet Halley 1985–1986, *Planet. Space Sci.*, *42*, 705, doi:10.1016/0032-0633(94)90111-2.

Yi, Y., R. J. Walker, T. Ogino, and J. C. Brandt (1996), Global magnetohydrodynamic simulation of a comet crossing the heliospheric current sheet, *J. Geophys. Res.*, *101*, 27,585, doi:10.1029/96JA02235.

Yoshizawa, A., and N. Yokoi (1996), Stationary large-scale magnetic fields generated by turbulent motion in a spherical region, *Phys. Plasmas*, *3*, 3604, doi:10.1063/1.871952.

Zhao, L., T. H. Zurbuchen, and L. A. Fisk (2009), Global distribution of the solar wind during solar cycle 23: ACE observations, *Geophys. Res. Lett.*, *36*, L14104, doi:10.1029/2009GL039181.